
Article:
Holt, J., Tadhunter, C., Morganti, R.. et al. (4 more authors) (2006) The co-evolution of the obscured quasar PKS 1549-79 and its host galaxy: evidence for a high accretion rate and warm outflow. Monthly Notices of the Royal Astronomical Society, 370 (4). pp. 1633-1650. ISSN 0035-8711

https://doi.org/10.1111/j.1365-2966.2006.10604.x

Mon. Not. R. Astron. Soc. **370,** 1633–1650 (2006) doi:10.1111/j.1365-2966.2006.10604.x

The co-evolution of the obscured quasar PKS 1549−79 and its host galaxy: evidence for a high accretion rate and warm outflow

J. Holt,[1] C. Tadhunter,[1⋆] R. Morganti,[2,3] M. Bellamy,[1] R. M. González Delgado,[4] A. Tzioumis[5] and K. J. Inskip[1]

[1]*Department of Physics and Astronomy, University of Sheffield, Sheffield S3 7RH*
[2]*ASTRON, PO Box 2, 7990 AA Dwingeloo, The Netherlands*
[3]*Kapteyn Astronomical Institute, University of Groningen, PO Box 800, 9700 AV Groningen, The Netherlands*
[4]*Instituto de Astrofisica de Andalucia, Apdto. 3004, 18080 Granada, Spain*
[5]*ATNF-CSIRO, Epping, Sydney, Australia*

Accepted 2006 May 23. Received 2006 May 18; in original form 2006 January 25

ABSTRACT

We use deep optical, infrared and radio observations to explore the symbiosis between nuclear activity and galaxy evolution in the southern compact radio source PKS 1549−79 ($z = 0.1523$). The optical imaging observations reveal the presence of tidal tail features which provide strong evidence that the host galaxy has undergone a major merger in the recent past. The merger hypothesis is further supported by the detection of a young stellar population (YSP), which, on the basis of spectral synthesis modelling of our deep Very Large Telescope (VLT) optical spectra, was formed 50–250 Myr ago and makes up a significant fraction of the total stellar mass (1–30 per cent). Despite the core-jet structure of the radio source, which is consistent with the idea that the jet is pointing close to our line of sight, our H I 21-cm observations reveal significant H I absorption associated with both the core and the jet. Moreover, the luminous, quasar-like active galactic nucleus (AGN) ($M_V < -23.5$) is highly extinguished ($A_v > 6.4$) at optical wavelengths and show many properties in common with narrow-line Seyfert 1 galaxies (NLS1), including relatively narrow permitted lines [full width at half-maximum (FWHM) ~ 1940 km s^{-1}], highly blueshifted [O III] $\lambda\lambda$5007,4959 lines ($\Delta V \sim 680$ km s^{-1}) and evidence that the putative supermassive black hole is accreting at a high Eddington ratio ($0.3 < L_{\rm bol}/L_{\rm edd} < 11$). The results suggest that accretion at high Eddington ratio does not prevent the formation of powerful relativistic jets.

Together, the observations lend strong support to the predictions of some recent numerical simulations of galaxy mergers in which the black hole grows rapidly through merger-induced accretion following the coalescence of the nuclei of two merging galaxies, and the major growth phase is largely hidden at optical wavelengths by the natal gas and dust. Although the models also predict that AGN-driven outflows will eventually remove the gas from the bulge of the host galaxy, the *visible* warm outflow in PKS 1549−79 is not currently capable of doing so. However, much of the outflow may be hidden by the material obscuring the quasar and/or tied up in hotter or cooler phases of the interstellar medium.

By combining our estimates of the reddening of the quasar with the H I column derived from the 21-cm radio observations, we have also made the first direct estimate of the H I spin temperature in the vicinity of a luminous AGN: $T_{\rm spin} > 3000$ K.

Key words: galaxies: formation – galaxies: individual: PKS 1549−79 – galaxies: interactions – quasars: general – galaxies: starburst.

1 INTRODUCTION

Powerful radio galaxies have long been considered as useful signposts to massive structures in the distant Universe. However, there is now increasing speculation that active galactic nuclei (AGN) and

⋆E-mail: c.tadhunter@sheffield.ac.uk (CT)

associated jet activity are not merely signposts but, in fact, are intimately linked to the galaxy evolution process. The main evidence for such links is twofold. On the one hand, the shape of the redshift evolution in the number density of quasars and radio galaxies shows marked similarities to that of the star formation history of the universe (Dunlop & Peacock 1990; Madau et al. 1996), while on the other hand close correlations have been found between the masses of the supermassive black holes that produce the prodigious nuclear activity and the properties of the bulges of the host galaxies (e.g. Tremaine et al. 2002).

The correlations between the redshift evolution of the radio source population and the star formation history of the field galaxy population can be explained in terms of hierarchical galaxy evolution models (e.g. Kauffmann & Haehnelt 2000). It is well known from the studies of nearby merging galaxies that stars are formed as part of the merger process. Numerical simulations of mergers of gas-rich galaxies also show that the tidal torques associated with the mergers concentrate gas in the circumnuclear regions of the galaxies (Barnes & Hernquist 1996; Mihos & Hernquist 1996); some of this gas may be available to fuel circumnuclear starburst, quasar and jet activity. Therefore, it is likely that AGN activity and near-nuclear starbursts in massive galaxies are a direct consequence of hierarchical galaxy evolution; AGN may be a symptom of the overall galaxy evolution process.

In this context, radio galaxies are key objects for understanding the link between star formation and AGN activity in individual galaxies. Not only is there clear morphological evidence that a significant subset of powerful radio galaxies – ∼50 per cent of those with strong emission lines – have undergone recent mergers (Heckman et al. 1986; Smith & Heckman 1989), but many of the radio galaxies with morphological evidence for mergers also show signs of recent star formation (Tadhunter, Dickson & Shaw 1996; Aretxaga et al. 2001; Tadhunter et al. 2002, 2005; Wills et al. 2002, 2004; Johnston et al. 2005). Despite these results, considerable uncertainties remain about the relationship between star formation and AGN/jet activity in radio galaxies. For example, it is not certain at what stage of the merger the AGN activity is triggered, nor whether the star formation is exactly coeval with the AGN activity. Indeed, some recent studies of the YSP in radio galaxies suggest that the activity may be triggered relatively late in the merger sequence, a significant time after the major episode of merger-induced star formation (Johnston et al. 2005; Tadhunter et al. 2005; Emonts et al. 2006). However, the sample sizes are currently small, and further detailed studies of the YSP in powerful radio galaxies are required to put our understanding of the link between star formation and AGN activity on a firmer footing.

While the links between star formation and AGN/jet activity provide evidence that AGN are a bi-product of the overall hierarchical galaxy evolution process, it has been suggested that the correlations between the supermassive black hole masses and the properties of the bulges of the host galaxies are a consequence of the feedback effects of AGN-induced outflows (Silk & Rees 1998; Fabian 1999; di Matteo, Springel & Hernquist 2005). To date, most of the evidence for such outflows has been provided by observations of narrow and broad absorption lines observed in the spectra of AGN at ultraviolet (UV) and X-ray wavelengths [see Crenshaw, Kraemer & George (2003) for a review]. The outflows associated with these absorption features clearly have an impact on the near-nuclear environments on a scale <10 pc, but the impact they have on the 1–10 kpc scale of galaxy bulges is less clear. Although outflows have also been detected in both ionized and neutral gas on a kpc-scale in powerful radio galaxies, uncertainties remain about the general importance of the outflows and their driving mechanism (quasars, jets or starbursts).

The subject of this paper – PKS 1549−79 – is a key object for studies of the links between galaxy evolution and AGN activity, because it shows clear evidence of both the merging process that may trigger the activity and the feedback effect of the AGN activity on the surrounding interstellar medium (ISM).

PKS 1549−79 is a compact flat spectrum radio source. Previously unpublished very long baseline interferometry (VLBI) radio images of the source show that it has the compact core-jet structure expected for such sources, consistent with the idea that its jet is pointing close to the line of sight. Remarkably for such a source, low-resolution optical spectra fail to reveal the broad permitted lines and strong non-stellar continuum characteristic of quasars and BL Lac objects (Tadhunter et al. 2001). Therefore, this object does not readily fit in with the simplest versions of the unified schemes which propose that lines of sight close to the radio axis have relatively unobscured views of the AGN (Barthel 1989).

Despite the absence of strong quasar continuum and broad emission line features, optical spectra of the source do reveal high-ionization forbidden emission lines which suggest that the source contains a powerful quasar-like AGN, even if this AGN is not directly visible at optical wavelengths. However, the high-ionization emission lines are unusually broad, and blueshifted by $\sim$650 km s^{-1} relative to the low-ionization lines. In addition, this object has H I 21-cm absorption detected against its radio core, at the same redshift as the low-ionization emission-line system. Further support for the idea that the quasar nucleus is obscured by the circumnuclear material in this source is provided by *K*-band spectroscopic observations that detect a broad Paα emission line and strong non-stellar continuum characteristic of quasars (Bellamy et al. 2003).

Apart from its unusual emission-line properties, PKS 1549−79 belongs to the subset of ∼30–50 per cent of powerful radio galaxies for which YSP make a substantial contribution to the optical continuum emission (Tadhunter et al. 2002). Further evidence for star formation in this object is provided by its unusually strong far-infrared (IR) emission, which leads to its classification as an ultraluminous infrared galaxy [ULIRG; see Sanders & Mirabel (1996) for a definition] with $L_{\rm ir} = 1.6 \times 10^{12}\,{\rm L}_{\odot}$. This evidence for recent star formation is consistent with the idea that the host galaxy of this source has been involved in a merger which has also triggered a major episode of star formation.

In this paper, we present new deep spectroscopic and imaging observations of PKS 1549−79 at optical, infrared and radio wavelengths that allow us to investigate the triggering of its AGN activity, characterize its circumnuclear outflows and deduce the nature of its AGN. In this way, we can place this key object in the context of evolutionary scenarios for the origin and evolution of the activity.

We assume cosmological parameters of $H_0 = 75$ km s^{-1} and $q_0 = 0.0$ throughout this paper. For these parameters, 1 arcsec corresponds to 2.39 kpc at the redshift of the host galaxy of PKS 1549−79.

2 OBSERVATIONS AND REDUCTIONS

2.1 Optical spectroscopy

Optical spectroscopic observations were taken in 2002 July and 2003 September using the ESO Multi Mode Instrument (EMMI) spectrograph in Red Imaging and Low Dispersion Spectroscopy (RILD) mode on the European Southern Observatory (ESO) 3.5-m New Technology Telescope (NTT), and the Visual and Near UV Focal Reducer and Low Dispersion Spectrograph 2 (FORS2)

Table 1. Log of optical and infrared observations for PKS 1549−79. In the case of the optical spectroscopic observations, the seeing was estimated from the seeing monitor estimates at the time of the observations, whereas for the imaging observations the seeing was measured directly from star images in the field of the source.

Date	Exposure (s)	PA	Slit width (arcsec)	Seeing FWHM (arcsec)
NTT/EMMI (Optical spectroscopy)				
02/07/12	3*1200(R)	−5	1.0	0.78
	3*1200(B)	−5	1.0	0.78
02/07/13	2*1200(R)	25	1.5	0.78
	2*1200(B)	25	1.5	0.78
VLT/FORS1 (Gunn r imaging)				
03/07/25	4*300	–	–	0.67
VLT/FORS2 (Optical spectroscopy)				
03/09/25	3*600(R)	75	1.3	1.2–1.8
03/09/25	3*1200(B)	75	1.3	1.2–1.8
AAT/IRIS2 (*K*-band spectroscopy)				
03/09/4	24*120	0	1.0	1.0
NTT/SOFI (*H*- and *K*-band spectroscopy)				
04/08/24	12*120	0	1.0	1.2

spectrograph in Long Slit Spectroscopy (LSS) mode on the ESO Very Large Telescope (VLT). Both sets of data are deeper and have a higher spectral resolution than those reported in Tadhunter et al. (2001). Details of the observations are given in Table 1.

On the NTT, grisms no. 5 and 6 were used with the MIT/LL mosaic to obtain spectra with wavelength ranges 3215–6136 and 4977–7565 Å in the blue and red, respectively. These configurations resulted in spectral resolutions of 5.0–6.7 Å in the blue and 4.2–5.6 Å in the red, depending on slit width. Red and blue exposures were interleaved in an attempt to ensure uniformity in conditions between the exposures. To reduce the effects of differential refraction, all exposures were taken with the slit aligned along the parallactic angle. Spectra were taken along two slit positions – PA 25 and PA −5.

The aim of the NTT spectra was to investigate the kinematics and physical conditions of the emission-line gas through the modelling of the bright emission lines. However, higher signal-to-noise ratio (S/N) is required to investigate the stellar populations in PKS 1549−79. Hence, we have also obtained optical spectra with the FORS2 spectrograph on the VLT on 2003 September 25. Grisms 600B and 600RI (holographic) were used with the MIT CCD to obtain spectra with wavelength ranges 3100–6000 and 5000–8200 Å respectively. The VLT spectra were taken with a 1.3-arcsec slit to ensure the entire nuclear region was sampled, and the slit was aligned along the parallactic angle (PA 75). The resulting spectral resolutions were 6.5 and 7.4 Å for the blue and red spectra, respectively. As with the NTT observations, the red and blue exposures were interleaved.

For both the NTT and the VLT observations, the data reduction followed the standard steps of bias subtraction, flat-fielding, wavelength calibration, atmospheric extinction correction, flux calibration and registration of blue and red spectral images. Based on measurements of night sky lines, the uncertainty in the wavelength calibration is estimated to be smaller than 0.5 Å for all data sets; the relative flux calibration uncertainty, based on the comparison of observations of several spectroscopic standard stars, is better than ±5 per cent. Prior to the analysis of the data, the spectra were corrected for a Galactic extinction assuming $E(B - V) = 0.679$ (Schlegel, Finkbeiner & Davis 1998) and the Seaton (1979) extinction law.

2.2 Optical imaging

Deep images of PKS 1549−79 were obtained using FORS1 on the VLT with a Gunn r filter in good seeing conditions (FWHM = 0.67 arcsec). The advantage of this filter is that, covering the rest wavelength range ∼5200–6100 Å, it avoids all strong emission lines in the source and is therefore dominated by continuum light. During the observations, the telescope was jittered to four separate positions on the sky to help remove cosmetic defects and average out sensitivity variations.

The imaging data were reduced using a combination of the STARLINK FIGARO package and IRAF by first subtracting the bias, dividing each separate frame by a jittered sky flat-field, and then combining the images with IMCOMBINE in IRAF using the coordinate information in the image headers.

2.3 Near-IR spectroscopy

In an attempt to improve on the near-IR spectroscopic data of Bellamy et al. (2003), which were affected by a faulty grism in IRIS2, new near-IR spectra of PKS 1549−79 were taken with the Anglo-Australian Telescope (AAT) and the NTT. Details of the observations are given in Table 1.

The first data set was obtained on 2003 September 4 using the IRIS2 instrument on the AAT. The Sapphire 240 grism was used to cover the *K* band. In total, 24 exposures of 120 s were obtained for PKS 1549−79, with the galaxy 'nodded' between two positions on the slit in an ABBA pattern. Four exposures of 66 s were taken of the A0 star HIP 77941 at a similar airmass for calibration purposes.

The second set was obtained on 2004 August 24 with the SOFI instrument on the NTT. The low-resolution red grism was used with the GRF order-sorting filter to cover the *H* and *K* bands simultaneously. Cloud was present during the night, and the observations were not photometric. 12 exposures of 120 s were obtained; the galaxy was again nodded along the slit, but this time with a random jitter every two exposures. Eight exposures of 30 s were taken of the A0 star HIP 79933 at a similar airmass for calibration purposes.

The IRIS2 exposures were co-added using median filtering to remove cosmic rays; the median 'B' image was then subtracted from the median 'A' image to remove the night skylines. The standard star frames were combined in a similar way. The resulting galaxy and star frames were then flat-fielded using a dark-subtracted flat-field taken with the same instrumental setup. The night skylines from the data frames themselves were used to determine a two-dimensional wavelength calibration, which was then applied to the final co-added frames of the galaxy and the standard star. The resulting spectra cover the range 20 320-24 900 Å. The spectral resolution, measured from the night sky lines, is 10.9 ± 0.4 Å (FWHM). Fits to the night sky lines show that the wavelength calibration is accurate to ±0.16 Å. The two-dimensional spectra were straightened using the APSUM package in IRAF, and one-dimensional spectra were extracted with FIGARO.

Night sky lines were also used to derive a wavelength calibration for the NTT data. The resulting two-dimensional transformation was then applied to all the individual data frames, and then suitable groups of exposures (because of the random jittering) were combined with FIGARO and a series of one-dimensional spectra was extracted and then combined together. There was no appreciable

tilting of the slit image and so the SOFI spectra did not need to be straightened before extraction. The SOFI spectrum covers the wavelength range 15 057-25 392 Å. Atmospheric absorption dominates between ∼18 000 and 19 500 Å and the thermal background dominates at wavelengths greater than ∼24 000 Å. The spectral resolution, measured from the arc lines, is 35.0 ± 0.4 Å (FWHM). Fits to the night skylines show that the wavelength calibration is accurate to ±0.77 Å.

The standard star exposures were used to remove telluric features and also to flux calibrate the IRIS2 spectra. The magnitude-to-flux conversion was performed with reference to Bessell, Castelli & Plez (1998), while telluric correction (and flux calibration for the IRIS2 data) was performed by assuming the intrinsic spectral energy distribution (SED) of the A0 stars to be that of a blackbody at T = 9480 K. For hot stars, this is a good approximation, particularly at the near-IR end of the blackbody spectrum. A number of Brackett lines are visible in the spectra of A0 stars, particularly in the H band, but these were masked out before the telluric correction was performed.

The SOFI data suffered unquantifiable slit-losses due to the telescope-nodding axis not being aligned precisely with the slit. For this reason, no attempt was made to make an absolute flux calibration of the SOFI spectrum. Instead, the spectrum was scaled to match the IRIS2 spectrum in the K band, and the spectrum of HIP 79933 was used only to remove telluric features and obtain the correct spectral shape.

2.4 Radio observations

Continuum VLBI observations of PKS 1549−79 were made at both 2.3 and 8.4 GHz with the Southern Hemisphere VLBI Experiment (SHEVE) network (Preston et al. 1993; Jauncey et al. 1994) between 1988 November and 1992 March using the MK2 recording system (Clark 1973). Full details of the antennae used for SHEVE observations are given in Tzioumis et al. (2002). The tapes recorded at each station were processed at the Caltech-JPL Block2 correlator in Pasadena, and the National Radio Astronomy Observatory (NRAO) AIPS package was used for global fringe fitting. The amplitude calibration and editing of the visibilities were subsequently performed using the Caltech-VLBI package. Self-calibration and imaging of the data were performed using DIFMAP (Shepherd, Pearson & Taylor 1994) and the AIPS packages. At 2.3 GHz, the restoring beams were 7.3 × 2.7 mas (PA 4.7) and 8.9 × 7.2 mas (PA 9.8) with and without the Hartebeesthoek antenna, respectively, whereas at 8.4 GHz the restoring beam was 6.7 × 5.2 mas (PA 73) without the Hartebeesthoek antenna. The rms noise in the final images is 2.7 mJy beam^{-1} at 2.3 GHz and 3.8 mJy beam^{-1} at 8.4 GHz.

In order to investigate the spatial distribution of the H I 21-cm absorption previously detected by Morganti, Oosterloo & Tadhunter (2001), H I VLBI observations were carried out using the Long Baseline Array (LBA) at the redshifted H I frequency of 1645 MHz. At this relatively low frequency, we could use only three telescopes: Parkes (64 m), Australia Telescope Compact Array (ATCA) Tied Array (5 × 22 m) and Mopra (22 m). We used a 16-MHz bandwidth in each circular polarization and 1024 channels. The final data cube (after Hanning smoothing) has a spectral resolution of ∼9 km s^{-1}, and a noise per spectral channel of 5.3 mJy beam^{-1}, while the continuum map derived from these data has a noise of 16 mJy beam^{-1}.

The editing part of the calibration of the 21-cm line data was done in AIPS and then the data were transferred to MIRIAD (Sault, Teuben & Wright 1995) for the bandpass calibration. The calibration of the bandpass was done using additional calibrations of the strong calibrators PKS 1718−649 and PKS 1934−638.

Both the line and the continuum image were made using uniform weighting, and the restoring beam is 47 × 32 mas (PA −77.3). As expected, the resolution is lower than that obtained in the previous VLBI continuum observations described above. The total cleaned flux in the continuum image is 4.75 Jy – close to that obtained from the previous low-resolution ATCA observations.

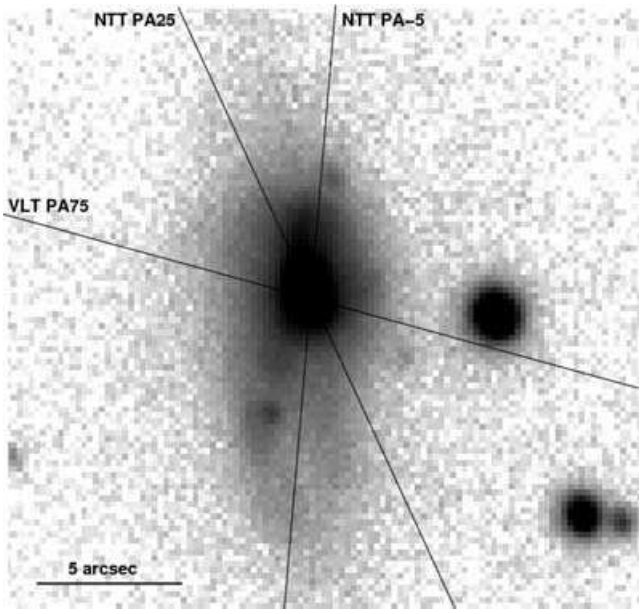

Figure 1. Deep VLT image of PKS 1549−79 taken with a Gunn r filter that avoids strong emission lines from the galaxy. The slit positions used for the long-slit spectroscopic observations are shown for reference. North is to the top and east to the left.

3 RESULTS

3.1 Optical imaging

Our deep VLT image of PKS 1549−79 is shown in Fig. 1. This reveals a disturbed optical continuum morphology, with a high surface brightness elongation extending 4 arcsec (10 kpc) to the north of the nucleus, a pair of tidal tails (or loop feature observed close to edge-on) extending a total distance of 10 arcsec (24 kpc) to the south and a fainter jet-like feature that extends 12 arcsec (29 kpc) to the north-north-east of the nucleus. The extended structures contain several knots of emission, particularly to the south-south-east and north-north-west. Overall, the structures suggest that PKS 1549−79 has undergone a recent merger, which induced star formation in the extended halo of the galaxy.

3.2 Optical spectroscopy

Three slit positions used for the optical spectroscopy observations are shown superimposed on the Gunn r image in Fig. 1.

3.2.1 Optical continuum modelling

Accurate modelling of the continuum is required not only to deduce the properties of any YSP present, but also as a prerequisite for accurate measurement of the emission lines, following subtraction

of the best-fitting continuum model. In this section, we concentrate on the VLT spectrum extracted for the nuclear region because this has higher S/N in the continuum than either of the NTT spectra.

Prior to continuum modelling, the level of the nebular continuum was deduced following the procedure outlined in Dickson et al. (1995) and Holt, Tadhunter & Morganti (2003), based on double Gaussian fits to the Hβ emission-line feature. This nebular continuum was then subtracted from the data. The major uncertainty in this procedure is the reddening in the nebular continuum. Unfortunately, estimates of the reddening using the Balmer lines are highly uncertain in this object (see Section 3.2.3). To consider the effects of the reddening of the nebular continuum on the results of the continuum modelling, we carried out the continuum modelling twice with two extreme sets of assumptions about nebular continuum. First, we assumed zero reddening for the nebular continuum. Second, we assumed the maximum reddening allowed by the Balmer line ratios.

The technique used to model the continuum is described in detail in Tadhunter et al. (2002, 2005). To summarize, the continuum flux is measured in several wavelength bins (in this case 39) chosen to avoid emission lines, cosmetic defects and poorly corrected atmospheric absorption features. A minimum χ^2 technique is then used to compare the measured fluxes with the results of spectral synthesis models. Models comprising various combinations of an old stellar population (12.5 Gyr), YSP (0.01–2.5 Gyr), reddened YSP [0.01–2.5 Gyr, $0.0 < E(B-V) < 2.0$] and a power law are compared with the data. For the spectral synthesis results, we used the most recent set of high-resolution models from Bruzual & Charlot (2003) for an instantaneous burst, a Salpeter initial mass function (IMF) and solar metallicity. For the reddened YSP, we used the Seaton (1979) extinction law to redden the YSP spectra from the spectral synthesis models. We also assumed a uniform uncertainty of ±5 per cent for all the measured fluxes, consistent with the estimated uncertainty of the relative flux calibration. Based on our experience of this modelling technique, models with $\chi^2_{\rm red} < 1$ can be deemed to provide a good fit to the data (see Tadhunter et al. 2005, for discussion).

In our first attempt to model the nebular-subtracted optical continuum, we considered the full wavelength range covered by the spectra. It became clear that no combination of old stellar population and YSP (reddened or otherwise) could fit the relatively steep rise in the spectrum to the red at wavelengths longer than ∼6500 Å and that a red power law is required to provide an adequate fit in that spectral range. Note that the steep rise to the red is not due to any problem with the reduction and calibration of the data, since it is also present in our NTT spectra. Fig. 2 shows the best-fitting model that comprises a 12.5 Gyr old stellar population, a 0.05 Gyr YSP reddened by $E(B-V) = 0.4$ and a power law. The level of the power-law component is consistent with the extrapolation of the reddened quasar continuum detected at near-IR wavelengths (see Section 3.3). Indeed, the existence of the red power law provides independent evidence for the partially extinguished quasar first detected by Bellamy et al. (2003).

In order to avoid the added uncertainly that the inclusion of a power law introduces into the modelling of the continuum, and to deduce an accurate age for the YSP, we then excluded wavelengths $\lambda > 6000$ Å from the model fits. In the case of maximum reddening for the subtracted nebular continuum, it is clear that the data are well fitted by models that include a combination of a 12.5 Gyr old stellar population and a YSP with age in the range 0.04–0.1 Gyr and reddening in the range $0.0 < E(B-V) < 0.75$, with a best fit obtained for a YSP age of 0.05 Gyr and reddening of $E(B-V) = 0.6$. The results appear to be robust in the sense that, if we assume that the nebular continuum suffers no reddening, the results are similar, except that the range of acceptable models extends to older ages for the YSP (0.05–0.25 Gyr) and the best-fitting model has an age of 0.1 Gyr and a reddening of $E(B-V) \sim 0.5$. The results of the SED modelling for the restricted wavelength range are shown in Fig. 3 for the zero reddening in the nebular continuum. The next step in the analysis was to check the SED fitting results by determining how well the models fit the profiles of absorption lines that do not suffer from significant emission-line contamination, namely the Ca II K, the *G* band and Mg I features. Reassuringly, the models that fit the general SED well also provide the best fits to the absorption lines. Fig. 4 shows an example of a fit to the optical spectrum for a model with a YSP of age 0.1 Gyr and reddening $E(B-V) = 0.5$, assuming zero reddening for the nebular continuum.

To summarize, fits to the optical continuum require a YSP with age in the range 0.04–0.25 Gyr and reddening $0.0 < E(B-V) < 0.8$ (depending on age) in order to provide an adequate fit to the optical SED and stellar absorption features. The YSP has a mass $2 \times 10^8 < M_{\rm ysp} < 4 \times 10^9$ M$_\odot$ and makes up 1–30 per cent of the total stellar mass in the slit (depending on the exact age and reddening). Note the age deduced for the YSP is significantly smaller than the 1 Gyr determined by Tadhunter et al. (2002) using lower resolution data with a narrower wavelength range. Much of this difference is likely to be due to the fact that Tadhunter et al. (2002) did not correct their spectrum for Galactic extinction prior to the modelling.

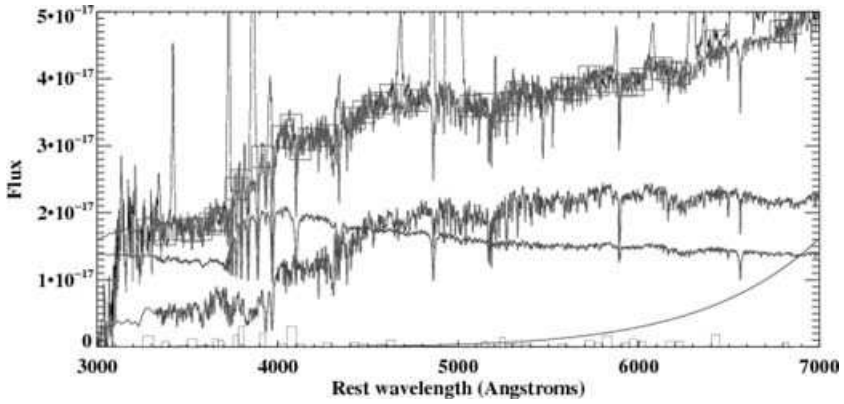

Figure 2. Spectral synthesis model fit to the full wavelength range of the optical spectrum of PKS 1549−79. The model comprises a 0.05 Gyr YSP reddened by $E(B-V) = 0.4$, a 12.5 Gyr old stellar population and a power law. Note that the power-law component is required to fit the steep rise in the continuum at the far-red end of the spectrum. The differences between the model and the data are presented as a histogram at the bottom of the plot.

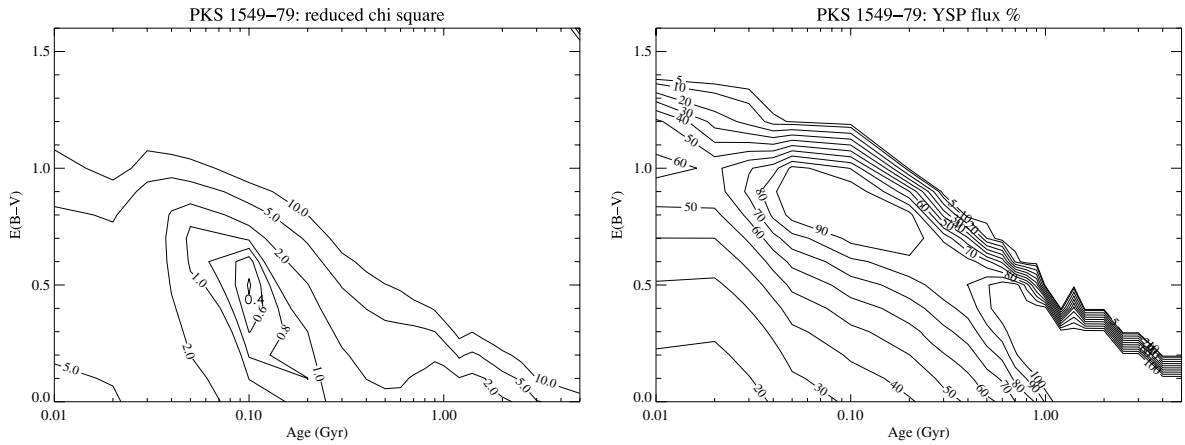

Figure 3. The results of minimum χ^2 fitting to the optical continuum of PKS 1549−79 assuming the zero reddening for the nebular continuum, restricting the wavelength range of the fits to $\lambda_{\rm rest} < 6000$ Å. The plot on the left-hand side gives the reduced χ^2 of the model fits for different combinations of YSP age and reddening, while the plot on the right-hand side gives the percentage contribution of the YSP component in the normalizing bin used for the modelling (4720–4820 Å). Reduced χ^2 values less than unity are deemed acceptable.

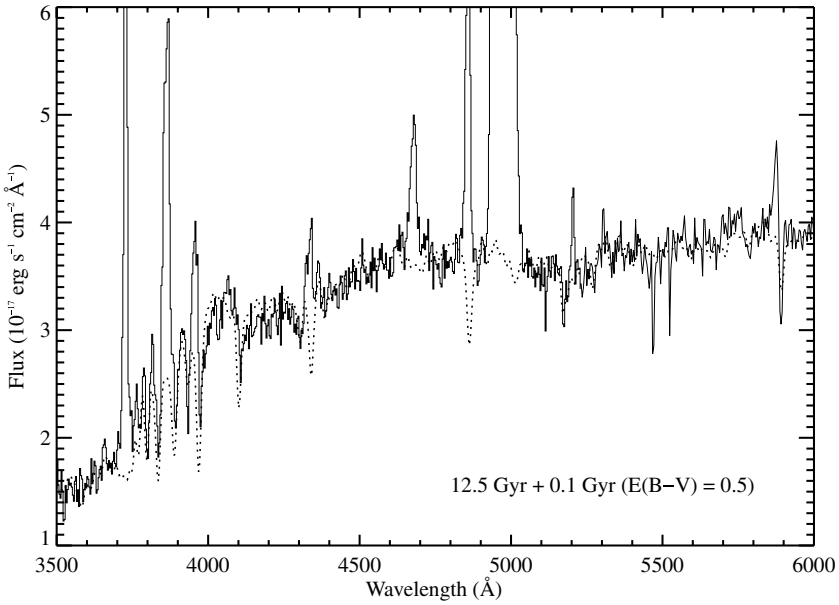

Figure 4. Example fit to the optical continuum for the model including a YSP with age 0.1 Gyr and reddening $E(B-V) = 0.5$ (zero reddening for the nebular continuum). The Ca II K, *G* band and Mg I absorption features are well fitted by this model, but the higher order Balmer lines are likely to suffer from residual emission-line contamination.

3.2.2 Emission-line kinematics

The long-slit spectra of PKS 1549−79 provide useful information on the emission-line kinematics in both the nuclear and off-nuclear emission-line regions. The spectra were measured by using the DIPSO package to fit Gaussian profiles to the lines. The velocity widths derived from the fits were quadratically corrected for the instrumental profile, and all linewidths and radial velocity shifts were corrected to the rest frame of PKS 1549−79.

The NTT spectra, which were obtained under good seeing conditions, provide the best information about the spatial extent and kinematics of the extended emission-line gas. Fig. 5 presents flux and radial velocity information derived from the fits to the emission-line profiles. The Hα emission line is detected across the full extent of the higher surface brightness continuum structures detected in the Gunn r continuum image shown in Fig. 1, extending 10 arcsec to the south and 5 arcsec to the north of the nucleus. The emission-line kinematics are relatively quiescent in the extended regions with small velocity amplitudes ($\Delta V < 150$ km s^{-1}) and linewidths (FWHM $<$ 400 km s^{-1}) – consistent with a gravitational origin for the gas motions (Tadhunter, Fosbury & Quinn 1989; Baum, Heckman & van Breugel 1990).

In contrast to the extended regions, the kinematics in the nuclear region provide evidence for more extreme gas motions, as already noted by Tadhunter et al. (2001). In order to analyse the gas motions in the spatially unresolved nuclear regions, we have adopted the approach used by Holt et al. (2003) for the radio galaxy, PKS 1345+12. This consists of fitting the minimum number of Gaussian components required to model each line adequately. For this analysis, we have concentrated on the VLT data which have a higher

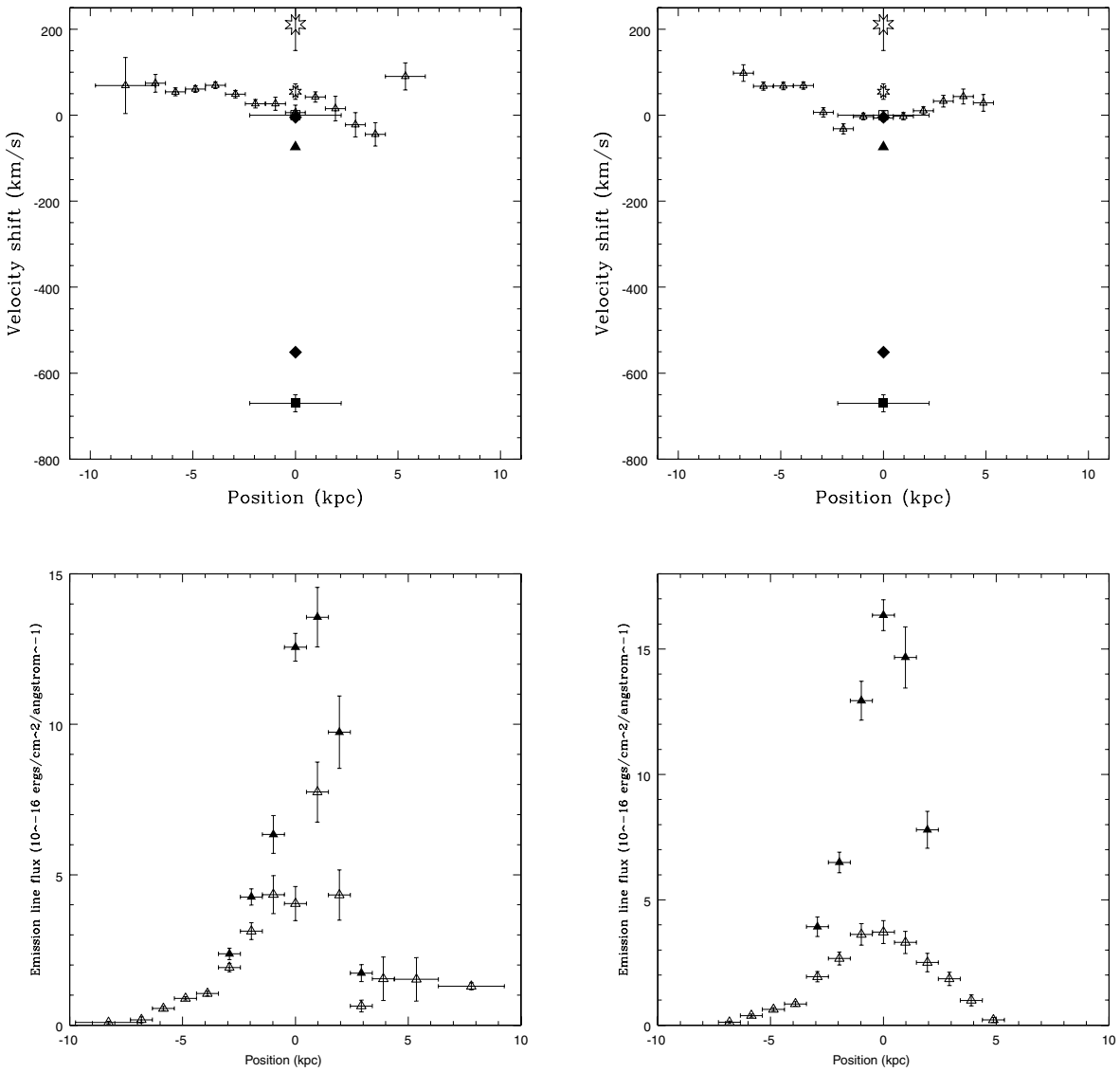

Figure 5. Radial velocity profiles (top) and the spatial variations of emission-line flux (bottom) for the NTT observations of PKS 1549−79. The left-hand images are for PA −5 and the right-hand images are for PA 25. Small open and filled triangles represent the narrow and intermediate components of Hα, respectively. Overplotted is the radial velocity of the deep H I 21-cm absorption [large filled triangle at −75 km s^{-1} from Morganti et al. (2001)], the shifts of the [O II] and [O III] lines from Tadhunter et al. (2001) (large filled diamonds at −5 and −550 km s^{-1}, respectively), the two components of the [O III] model in the nucleus (large open and filled squares) and the broad components of Paα listed in Table 2 (open eight-pointed stars). For PA −5, positive positions are to the north and negative positions are to the south. For PA 25, positive positions are to the SSW and negative positions are to the NNE.

S/N in the nuclear regions. In the case of emission-line doublets ([O III] $\lambda\lambda$5007,4959, [O I] $\lambda\lambda$6300,6363, [N II] $\lambda\lambda$6548,6584, [S II] $\lambda\lambda$6717,6731), the separations and, with the exception of the [S II] blend, the ratios of the lines were set by atomic physics, and it was assumed that both components of the doublets have the same kinematic components. We found that for all the low-ionization lines [O II] λ3727, Hβ, [O I] $\lambda\lambda$6300,6363, [N II] $\lambda\lambda$6548,6584 and [S II] $\lambda\lambda$6717,6731, a double Gaussian fit comprising narrow (FWHM < 400 km s^{-1}) and intermediate width blueshifted components (FWHM > 1000 km s^{-1}) provided an adequate fit to the emission-line profiles. For these low-ionization lines, the narrow component is strongest, and the widths and redshifts of the narrow components are consistent within the uncertainties for all the narrow lines; they are also consistent with the redshift of the Hα emission line detected in the extended regions (see Fig. 5). The intermediate emission-line component is relatively weak in the low-ionization lines, and its width and redshift less well determined based on free double Gaussian fits.

Initial attempts to fit the [O III] $\lambda\lambda$5007,4959 lines showed that it was possible to fit each of line of the doublet adequately using a single Gaussian component that is both broad and blueshifted relative to the narrow component detected in the low-ionization lines (see also Tadhunter et al. 2001). However, given that results obtained for [O III] in apertures slightly offset from the nucleus show the clear presence of a narrow (FWHM < 400 km s^{-1}) emission-line component that is also detected in the low-ionization lines, we have also fitted each component of [O III] doublet in the nucleus using a double Gaussian model, with one of the Gaussian components constrained to have the velocity width and redshift of the narrow component detected in the low-ionization lines. The resulting

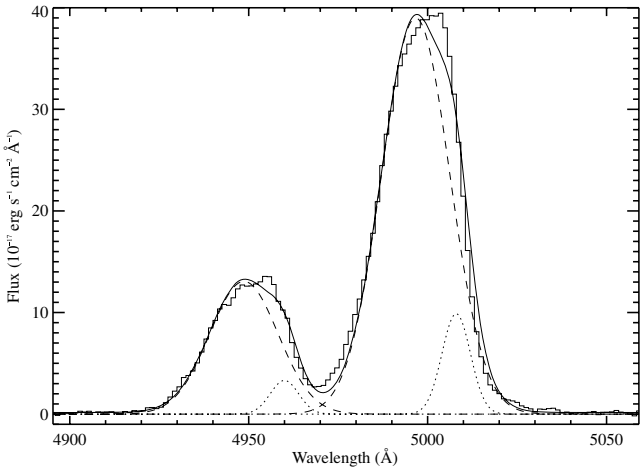

Figure 6. Double Gaussian model for the [O III] λλ4959,5007 doublet in the nucleus, forcing the redshift of the narrow component to be consistent with the redshift of the narrow component in the low-ionization lines. The composite model is overplotted (bold line) on the extracted spectrum (faint line). All of the four components (two for each line) are also plotted: the dotted lines trace the narrow components and the dashed lines trace the broad components.

fit – comprising the narrow component and an intermediate, blueshifted component – is shown in Fig. 6. The imperfections of this fit in the line cores are to likely reflect the fact that a single Gaussian is only an approximation to the true profile of the intermediate, blueshifted component in the nucleus. Note that such imperfections would not be apparent in fits to the low-ionization lines, because of the weakness of the broad components and the dominance of the narrow components in such lines.

Following on from the double Gaussian fits to [O III], we then attempted to fit all the emission lines in the nuclear regions with a double Gaussian model comprising the following two components.

(i) A narrow component (FWHM = 383 ± 15 km s^{-1}) with redshift $z = 0.152\,25$, measured from double Gaussian fits to the bright low-ionization lines.

(ii) An intermediate component (FWHM = 1282 ± 25 km s^{-1}) blueshifted by 679 ± 20 km s^{-1} with respect to the narrow component, measured from double Gaussian fits to the [O III] lines.

This model provides an adequate fit to all the lines in the nuclear emission spectrum, with the following notable exceptions.

(i) The Hα+[N II] blend requires an additional broad Hα emission-line component to fit the wings of the blend. We find that we can obtain an adequate fit to the blend if we set the width and redshift of the broadest Hα component to be the same as those deduced from single Gaussian fits to the broad Paα line detected by Bellamy et al. (2003, $z = 0.152\,38$, FWHM = 1940 km s^{-1}). The flux measured for the broadest Hα component is 4.2×10^{-15} erg cm^{-2} s^{-1}. The detection of this component provides further evidence that the reddened quasar nucleus is detected at the longer wavelength end of the optical window.

(ii) The faint high-ionization lines [Ne V] λ3425 and [Fe VII] λ6087 could be fitted adequately by the intermediate component alone, whereas the faint low-ionization [N I] λ5200 could be fitted by the narrow component alone. Presumably, in each of these cases the other component that would otherwise be detected in a double Gaussian fit is not detected because of the low S/N and uncertainties in the continuum subtraction.

Table 2. Comparison of the redshifts and linewidths of the various kinematic components detected in the nuclear regions of PKS 1549−79. Results for nuclear narrow and intermediate components are based on double Gaussian fits to the optical emission lines detected in the VLT spectrum, while the Paα results are based on double Gaussian fits to the Paα feature detected in the new AAT *K*-band spectrum.

Component	Redshift	Linewidth(FWHM) (km s^{-1})
Nuclear narrow	0.152 25 ± 0.000 03	383 ± 15
Nuclear intermediate	0.149 59 ± 0.000 03	1282 ± 25
Paα core	0.152 38 ± 0.000 06	1250 ± 70
Paα broadest	0.1529 ± 0.0002	3525 ± 200
H I 21-cm narrow	0.151 95 ± 0.000 06	80 ± 30

The velocity shifts and widths of the various kinematic components detected in PKS 1549−79 are compared in Fig. 5 and Table 2. Not surprisingly, the intermediate and narrow components in the double Gaussian fits have similar redshifts and linewidths to the high- and low-ionization lines measured in single Gaussian fits to the lower resolution data of Tadhunter et al. (2001). It is notable that both the width and velocity shift of the nuclear narrow component are consistent with those deduced for the extended Hα emission on both sides of the nucleus; the redshift of this component is also close to that measured for both the core of the broad Paα line and the narrow H I absorption (see below). Therefore, we identify the nuclear narrow component with the rest frame of the host galaxy, and the intermediate component detected most clearly in the [O III] lines with a highly disturbed component that is blueshifted relative to this rest frame.

3.2.3 Ionization and physical conditions

Given the success of the two-component emission-line profile described in the last section, it is possible to investigate the ionization, reddening and physical conditions for the narrow and intermediate emission-line components detected in the nuclear aperture separately. The emission-line ratios for both of the components derived from the double Gaussian profile fits are shown in the third column of Table 3. In addition to the nuclear aperture, Table 3 also shows emission-line ratios determined for a 1.3 × 1.3 arcsec^2 aperture centred 1.6 arcsec to the east of the nucleus along PA 75 (AP1; VLT spectrum). In the case of this extended aperture, which is affected by seeing disc spillover of the nuclear emission-line flux, it proved necessary to use a double Gaussian fit to model the lines accurately – one component representing the nuclear intermediate component and the other the extended narrow component. However, despite the contamination by the nuclear flux in this aperture, the narrow component has a much better contrast relative to the intermediate component than in the nuclear aperture; in Table 3 we only list the narrow-line ratios for this aperture.

It is immediately clear from Table 3 that the blueshifted, intermediate component detected in the nucleus is characterized by a high-ionization state, with relatively strong [Ne V], [Ne III], He II,

Table 3. Data for all optical emission lines detected in the nuclear and extended apertures of PKS 1549−79. Columns are (a) emission line; (b) emission-line component where N and I are the narrow and intermediate components; (c) emission-line fluxes measured for a 1.3 × 1.3 arcsec^2 aperture centred on the nucleus, extracted from the PA 75 VLT data (fluxes expressed relative to Hβ); (d) emission-line fluxes measured for a 1.3 × 1.3 arcsec^2 extended aperture centred 1.6 arcsec east of the nucleus, extracted from the PA 75 VLT data.

Emission line	Comp.	Nuclear flux	Extended flux
(*a*)	(*b*)	(*c*)	(*d*)
[Ne V] 3425.9	N	–	<20
	I	75 ± 8	–
[O II] 3727.64†	N	330 ± 30	420 ± 50
	I	38 ± 8	–
[Ne III] 3868.8	N	50 ± 8	80 ± 10
	I	110 ± 8	–
[Ne III] 3968.4	N	18 ± 3	26 ± 4
	I	38 ± 4	–
Hγ 4339.95	N	33 ± 4	–
	I	27 ± 3	–
[O III] 4363.2	N	8 ± 3	<22
	I	<8	–
He II 4685.75	N	11 ± 4	20 ± 10
	I	52 ± 7	–
Hβ 4860.75	N	100	100
	I	100	–
[O III] 4958.9	N	140 ± 10	150 ± 30
	I	580 ± 45	–
[O III] 5006.9	N	410 ± 50	450 ± 80
	I	1700 ± 150	–
N I 5199.1	N	51 ± 6	–
	I	<10	–
He I 5875.2	N	64 ± 8	–
	I	<10	–
[Fe VII] 6086.0	N	<10	–
	I	42 ± 5	–
[O I] 6300.3	N	160 ± 20	80 ± 10
	I	57 ± 10	–
[O I] 6363.8	N	53 ± 6	28 ± 4
	I	15 ± 4	–
[N II] 6548.09	N	420 ± 30	180 ± 20
	I	190 ± 20	–
Hα 6562.9	N	400 ± 50	500 ± 70
	I	350 ± 40	–
[N II] 6583.36	N	1230 ± 100	560 ± 70
	I	570 ± 100	–
[S II] 6716.4	N	290 ± 15	120 ± 20
	I	20 ± 4	–
[S II] 6730.8	N	270 ± 15	140 ± 20
	I	47 ± 10	–
F(Hβ)	N	2.4×10^{-16}	0.9×10^{-16}
(erg cm^{-2} s^{-1})	I	5.4×10^{-16}	–

†Weighted mean of [O II] doublet at the low density.

[O III] and [Fe VII] lines, and relatively weak [O II], [O I] and [S II] lines.

In contrast, the ionization state of the narrow component detected in both the nuclear and extended apertures is relatively low, with [O II], [O I], [N II] and [S II] all strong relative to the higher ionization [Ne V], [Ne III] and He II and [O III] lines.

On the basis of the Hα/Hβ ratio alone, there is no strong evidence for a high degree of reddening affecting the narrow-line region (NLR) in this object, in contrast to the situation in PKS 1345+12 – an object that also shows broad, blueshifted Balmer lines (Holt et al. 2003). However, it is difficult to be entirely confident of the accuracy of the Hα flux because of the complexity of the seven Gaussian model required to fit the Hα+[N II] blend. Moreover, the higher order Balmer lines cannot be used to check the reddening estimated from Hα/Hβ because of their weakness relative to the continuum and underlying Balmer absorption-line features. Given these uncertainties, we have made no attempt to correct the emission-line ratios for reddening.

Similarly, it has not been possible to estimate accurate electron temperatures for the narrow-line gas using the [O III](5007+4959)/4363 line ratio, because the faint [O III] λ4363 line is highly sensitive to the accuracy of the continuum subtraction, particularly for the broader, blueshifted component that is also blended with Hγ. None the less, it has been possible to estimate the electron density from the [S II](6731/6717) ratio for the narrow emission-line component detected in the nuclear aperture and the extended aperture along PA 75. Using a model for the [S II] λλ6717,6731 blend that includes both an intermediate blueshifted component and a narrow component for each line in the doublet, and assuming an electron temperature of 10 000 K for the region emitting the [S II] lines, we estimate an electron density 430 ± 50 cm^{-3} for the narrow component in the nuclear aperture. Unfortunately, because of the relative weakness of the intermediate blueshifted component to the lines, the electron density in the gas emitting the blueshifted component is not well-constrained by these observations. We find that, although four Gaussian models with the doublet ratios left unconstrained tend to the high-density limit for the intermediate component, models with the ratio of the intermediate component fixed at the low-density limit also provide adequate fits to the blend. On the other hand, the ratios determined for the narrow components are not sensitive to the details of the model used for the intermediate components.

In order to investigate the ionization mechanism(s) for the various kinematic components, the emission-line ratios are compared with various ionization models and the results for other radio galaxies in the four diagnostic diagrams presented in Fig. 7. Four sets of models are plotted: single-slab optically thick power-law photoionization models calculated using the MAPPINGS code; mixed medium photoionization models taken from Binette, Wilson & Storchi-Bergmann (1996); pure shock cooling zone models and shock plus precursor models from Dopita & Sutherland (1995, 1996).

These diagnostic diagrams further emphasize the high-ionization character of the gas emitting the intermediate, blueshifted component. In all diagnostic diagrams except that involving [N II], the line ratios for this component can only be fitted with power-law AGN photoionization models that have a high-ionization parameter ($0.05 < U < 0.1$), and the line ratios are most consistent with models that have a power-law spectral index of −1.5. Although the particular mixed medium photoionization models plotted in the diagrams do not provide a good fit to the line ratios of the intermediate component, it is possible that, by changing the parameters of such models (e.g. ionization parameter, column depth of matter bounded component), an acceptable fit could be obtained. It is also notable that none of the shock or shock+precursor can provide an adequate fit to the line ratios.

The intermediate component has line ratios that place it beyond the high-ionization end of the locus of narrow-line radio galaxies, overlapping with the range of ionization parameter measured for the narrow, blueshifted absorption-line systems detected against

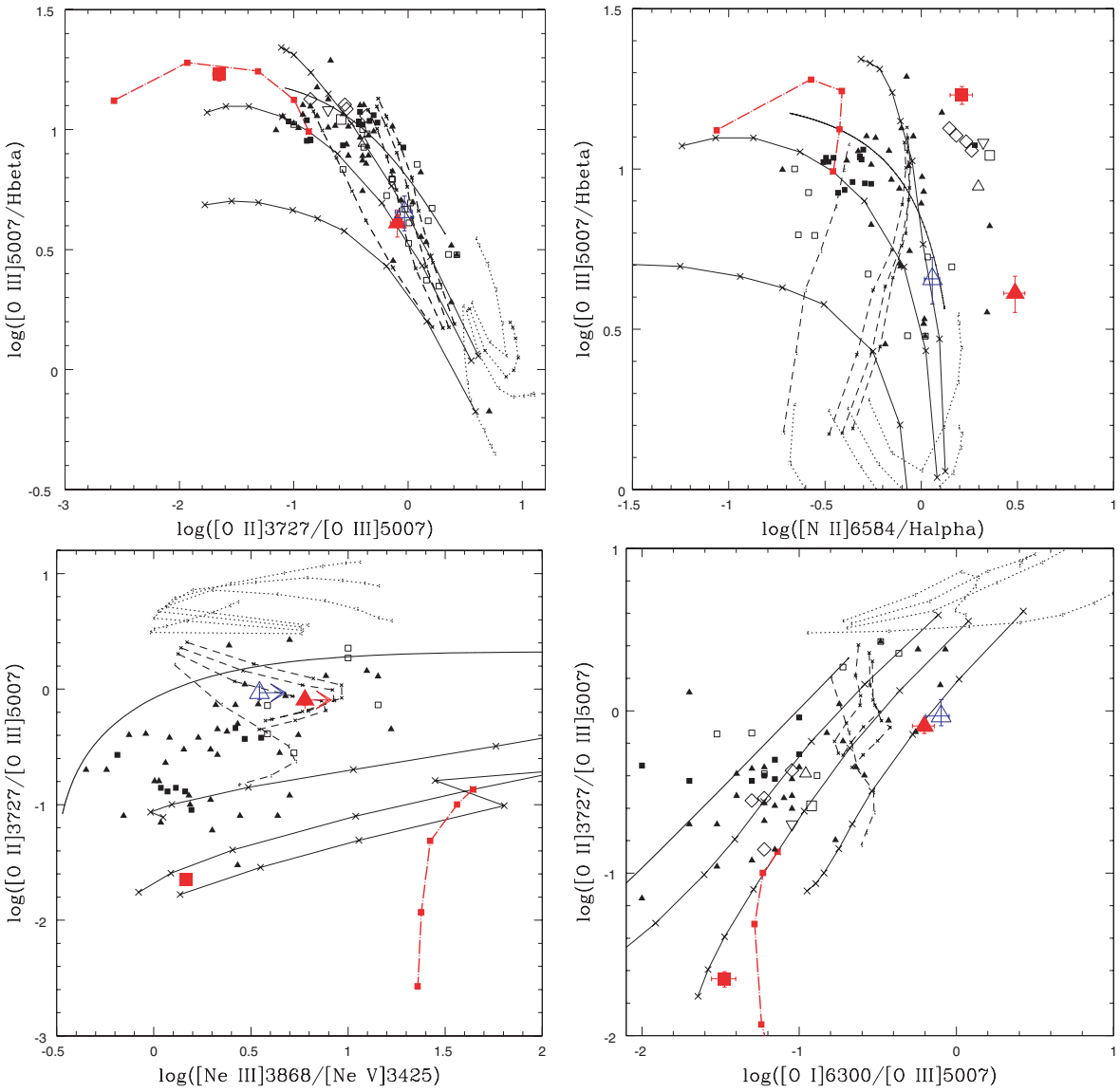

Figure 7. Emission-line diagnostic diagrams for PKS 1549−79. Upper left: [O III]/Hβ versus [O I]/[O III]. Upper right: [O III]/Hβ versus [N II]/Hα. Bottom left: [O II]/[O III] versus [Ne V]/[Ne III]. Bottom right: [O III]/[O II] versus [O I]/[O III]. In these diagrams, the pure shock models of Dopita & Sutherland (1996) for a range of magnetic parameter ($B/\sqrt{n} = 0$, 1, 2 μG cm$^{3/2}$) with shock velocities $150 \leqslant v_{\rm shock} \leqslant 500$ km s^{-1} are represented by dotted lines, while the shock plus precursor models are represented by dashed lines. Solid lines represent optically thick power law ($F_\nu \propto \nu^\alpha$) photoionization models calculated using the MAPPINGS code for three power-law spectral indices ($\alpha = -1.0$, -1.5, -2.0) for a sequence in the ionization parameter ($2.5 \times 10^{-4} \leqslant U \leqslant 10^{-1}$) increasing from right- to left-hand side. Most of the photoionization models plotted in these figures were calculated for low electron densities ($N = 10^2$ cm^{-3}); however the red dot–dashed lines show a sequence of models calculated at a single ionization parameter ($U = 5 \times 10^{-3}$) for a range of densities ($10^2 < N < 10^6$ cm^{-3}). The bold line corresponds to mixed-medium models from Binette et al. (1996) that include both matter- and ionization-bounded clouds for a range of ratios of the solid angles covered by the matter- and ionization-bounded clouds ($10^{-2} \leqslant A_{M/I} \leqslant 10$) increasing from right- to left-hand side. The nuclear intermediate component is represented by the large red solid square, while the narrow components for the nuclear and extended apertures are represented by large red solid and open blue triangles, respectively. For comparison, the small filled triangles represent data for the nuclear NLRs of radio galaxies (data from Costero & Osterbrock 1977; Cohen & Osterbrock 1981; Grandi & Osterbrock 1978; Clark 1996; Storchi-Bergmann et al. 1996; Dickson 1997; Villar-Martin et al. 1998; Solorzano-Innarea 2001; Robinson et al. 2000; Wills et al. 2002), small filled squares represent extended emission-line regions (data from Morganti et al. 1991; Tadhunter et al. 1994; Storchi-Bergmann et al. 1996; Robinson et al. 2000) and open squares represent EELRs with strong jet–cloud interactions (data from: Clark 1996; Clark et al. 1998; Villar-Martin et al. 1998, 1999; Solorzano-Innarea 2001). On addition, we present the line ratios for various kinematic components detected in the spatially resolved NLR of Cygnus A by Taylor et al. (2003), with the nuclear broad and narrow components plotted as small open triangles, and the extended narrow components plotted as open diamonds.

the UV and X-ray continua of Seyfert 1 galaxies and quasars (Crenshaw et al. 2003). Indeed, we would expect such absorption-line systems to be detected in PKS 1549−79 for lines of sight to the AGN that intercept the high-ionization gas. The only line ratio that does not fit in with this general trend is [N II]/Hα, which is unusually large considering the high-ionization state revealed by the other lines. This may reflect the fact that the systematic uncertainties for this ratio are larger than for the others because of the complexity of the Hα+[N II] blend. Moreover, the models plotted in Fig. 7 assume Solar elemental abundance ratios, whereas the abundance of

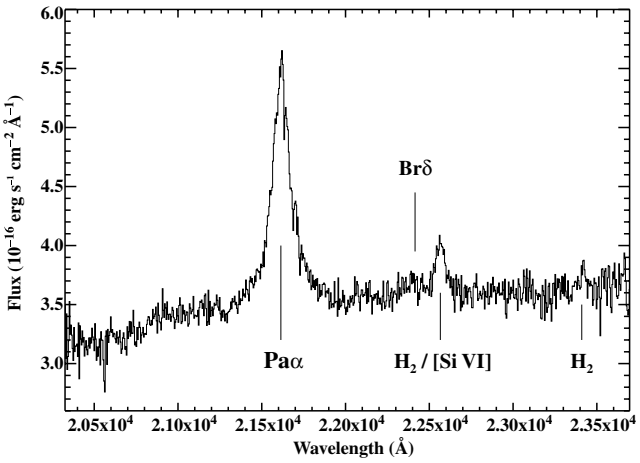

Figure 8. Near-IR (*K* band) spectrum of PKS 1549−79 taken using the IRIS2 spectrograph on the AAT. The main spectral features are marked. At near-IR wavelengths, the spectrum is dominated by a quasar component.

nitrogen relative to other elements such as oxygen may be significantly larger than the Solar value – the favoured explanation for the unusually strong [N II] in, for example, Cygnus A (Tadhunter, Metz & Robinson 1994).

The diagnostic diagrams also show that the line ratios of the narrow emission-line components (all apertures) fall at the lower ionization end of the ratios measured for the NLRs of radio galaxies in general, consistent with photoionization at moderate ionization parameter, or shock+precursor ionization models. Despite the evidence for YSP in this source, and the possibility of on-going star formation, the strengths of the [O I] and [N II] emission lines relative to Hα preclude H II region-like photoionization by normal OB stars.

3.3 Near-IR spectroscopy

Our new deep *K*-band spectrum of the nuclear regions taken with the ATT/IRIS2 is shown in Fig. 8. This represents a substantial improvement over the previous *K*-band spectrum published in Bellamy et al. (2003), which was affected by a faulty grism that resulted in splitting of all spectral features. As well as the strong Paα emission line, the spectrum shows a feature near 2.26 μm that is likely to represent a blend of $H_2\nu = 1 - 0$S(3) and [Si VI] λ1.963 μm, an $H_2\nu = 1 - 0$S(2) line and (less certainly) a broad feature close to the expected wavelength of redshifted Brδ.

The Paα feature can be modelled as a combination of two Gaussians of width 1220 ± 90 and 3540 ± 320 km s^{-1} (FWHM) with fluxes of (1.10 ± 0.16) × 10^{-14} and (1.92 ± 0.15) × 10^{-14} erg cm^{-2} s^{-1}, respectively; redshifts for these components are given in Table 2. Similar results are obtained from fitting our NTT/SOFI spectrum. Although the narrower of these two broad components has a width similar to that of the intermediate component detected in the [O III] lines, its redshift is close to that of the narrow emission-line components (see Table 2); therefore it cannot be emitted by the same gaseous system that emits the intermediate [O III] line component. Given this, and the fact that the broader Paα component has a width that falls outside the normal range for the narrow-line gas associated with AGN, it is likely that the Paα line is dominated by genuine broad line region (BLR) emission. For comparison, a single Gaussian fit to the Paα gives a linewidth: FWHM = 1940 ± 50 km s^{-1}.

The new spectra also allow us to resolve the uncertainty in the identification of the feature at ∼ 2.26 μm in the observed spectrum (see Fig. 8). In terms of its redshift, this feature could be identified either with blueshifted [Si VI] λ1.963 μm or with $H_2\nu = 1 - 0$S(3) at the redshift of the nuclear narrow component. However, a single Gaussian fit to this feature gives a width of 970 ± 80 km s^{-1}, which is significantly broader than the nuclear narrow component, but significantly narrower than the intermediate component, suggesting that the feature is composite. Therefore, we have attempted a double Gaussian fit to the feature with one Gaussian component representing $H_2\nu = 1 - 0$S(3) with the same width and redshift as the nuclear narrow component, and the other representing [Si VI] λ1.963 μm with the same width and redshift as the nuclear intermediate component. This double Gaussian model provides a good fit to the data with fluxes of (4.5 ± 1.5) × 10^{-16} erg cm^{-2} s^{-1} and (3.1 ± 0.3) × 10^{-15} erg cm^{-2} s^{-1} for the narrow $H_2\nu = 1 - 0$S(3) and intermediate [Si VI] λ1.963 μm components, respectively. The detection of $H_2\nu = 1 - 0$ S(3) is consistent with the presence of $H_2\nu = 1 - 0$S(2) in the spectrum at longer wavelengths; the estimated luminosity for the $H_2\nu = 1 - 0$S(3) line (2.3 × 10^{40} erg s^{-1}) is less than estimated by Bellamy et al. (2003) who assumed that all the ∼ 2.26 μm feature is $H_2\nu = 1 - 0$S(3). It is notable that the detection of the blueshifted [Si VI] λ1.963 μm line is consistent with the high-ionization character of the intermediate emission-line component deduced from the optical observations (see Section 3.2).

Along with information about the emission-line systems, the new spectra provide key information about the quasar continuum emission. In particular, the new NTT spectrum has a broader spectral coverage than the AAT/IRIS spectra and allows more stringent limits to be placed on the reddening to the AGN. To estimate the AGN reddening, we follow the same technique as Bellamy et al. (2003): fitting the near-IR continuum spectrum assuming a range of intrinsic power-law optical-infrared spectral shapes for quasars taken from Simpson & Rawlings (2000). The results are presented in Table 4 and Fig. 9.

On the basis of this modelling alone, it is clear that the *V*-band absorption and absolute magnitude of the AGN must fall in the range $4.9 < A_v(\text{intrinsic}) < 13.2$ and $-27.56 < M_v < -22.64$, respectively. However, the recent *Hubble Space Telescope* (*HST*)/Advanced Camera for Surveys (ACS) imaging of PKS 1549−79 (Batcheldor et al., in preparation) allows us to place a stringent

Table 4. Reddening and absolute magnitude estimates for the quasar nucleus in PKS 1549−79. The second, third and fourth columns give the minimum, average and maximum reddening corresponding to the range of optical/UV power-law slopes deduced by Simpson & Rawlings (2000). The second row gives the values of the assumed spectral index for the intrinsic optical-IR spectral shape (convention: $F_\nu \propto \nu^{-\alpha}$). The final four rows give estimates for the $E(B-V)$ reddening, A_v extinction and the estimated absolute magnitude of the quasar nucleus in both the *V* and the *K* bands. In modelling the continuum shape, we have assumed the extinction law of Rieke & Lebofsky (1985).

	Minimum	Average	Maximum
α(intrinsic)	1.62	0.90	−0.67
$E(B-V)$	1.52	2.31	4.04
A_v	4.94	7.52	13.19
M_v	−22.64	−24.18	−27.56
M_k	−26.97	−27.43	−28.44

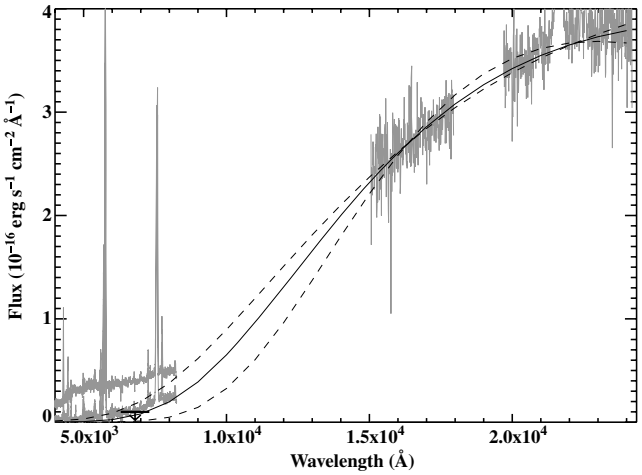

Figure 9. Fit to the shape of the near-IR H+K spectrum of PKS 1549−79 taken on the NTT, showing the extrapolation to optical wavelengths for various assumptions about the power-law shape of the optical-IR continuum. Also shown are the VLT optical spectrum (upper curve at short wavelengths), and the VLT spectrum following subtraction of the best-fitting stellar continuum model (lower curve at short wavelengths). The upper and lower dashed lines represent models with the minimum and maximum reddening, respectively, while the solid line represents the average reddening case (see Table 4). The arrow in the lower left corner of the plot represents the upper limit on the AGN continuum flux at 5900 Å derived from *HST* imaging observations.

upper limit on the flux of the quasar core at 5900 Å (rest) of $F_\lambda < 1.0 \times 10^{-17}$ erg cm^{-2} Å^{-1}. Using this limit, it is clear from Fig. 9 that the intrinsic absorption and luminosity of the quasar must lie at the upper end of the range predicted on the basis of the near-IR continuum modelling; we find that the optical flux limit implies $A_v > 6.4$, $M_V < -23.5$ and $M_K < -27.3$. This places the AGN in PKS 1549−79 firmly in the luminosity range of quasars ($M_v < -23.0$). Note also that such high values of nuclear extinction and luminosity are consistent with the residual spectrum obtained by subtracting the best-fitting stellar continuum model from our VLT spectrum (see Fig. 4).

3.4 Radio imaging and spectroscopy

3.4.1 VLBI continuum imaging

Fig. 10 shows the VLBI images made with SHEVE at 2.3 and 8.4 GHz. The radio source is characterized by a compact core to the western extreme of the source, which shows a jet-like extension in PA 64, and a highly collimated jet structure to the east aligned along PA 120. The overall extent of the source in the 2.3 GHz image is 180 mas (430 pc), and there is no strong evidence for emission from more extended structures; >95 per cent of the total (single dish) flux is contained within the structures visible in the VLBI images. Relative to the western core, the jet appears significantly fainter in the 8.4-GHz image (core/jet ratio ∼10:1) than it does in the 2.3-GHz image (core/jet ratio ∼2:1), but the western core has a similar brightness in both the images. The non-simultaneity of the 2.3 and 8.4 GHz VLBI data and the resolution differences between the two frequencies preclude accurate determination of the power-law spectral indices of the jet and core components. However, the data are consistent with a steep spectrum for the jet ($\alpha \sim -1.2$; $F_\nu \propto \nu^{+\alpha}$) and a much flatter spectrum ($\alpha \sim 0$) for the core.

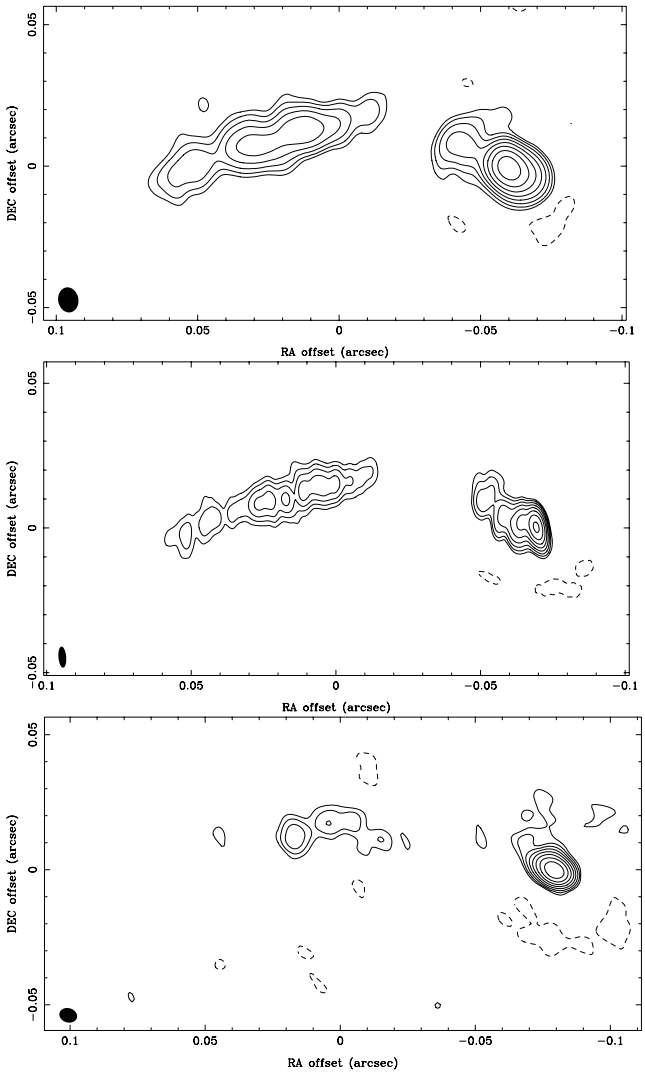

Figure 10. High-resolution VLBI radio maps of PKS 1549−79. The upper map is for a frequency of 2.3 GHz excluding the Hartebeesthoek antenna, the middle map is also for a frequency of 2.3 GHz but including the Hartebeesthoek antenna, while the lower map is for an observation frequency of 8.4 GHz (contours: −10, 10, 20, 40, 80, 160, 320, 640 and 1280 mJy Beam^{-1}).

Note that the total flux recovered in our VLBI observations at 8.4 GHz (3.6 Jy – data taken in 1991) is significantly larger than the 8.4-GHz flux measured more recently by Drake et al. (2004b, 2.4 Jy – data taken between 1996 and 1998). This suggests that the core is variable at high frequencies.

Overall, the radio structure is similar to the core-jet structures detected in some other radio-loud quasars such as 3C273. Such structures are generally interpreted in terms of radio emission from a two-sided relativistic jet structure, with the axis of jets pointing close to our line of sight. In this case, the radio emission from the jet on the near side is enhanced because the radio emission is beamed towards the observer, whereas the emission from the jet on the far side is dimmed because the radiation is beamed away from the observer. The significant curvature in the jet is also consistent with the beaming hypothesis, since a small degree of intrinsic jet curvature will be exaggerated if the jet is pointing close to the line of sight. If this beaming/orientation explanation for the one-sided jet is correct, then the total radio emission from the source will

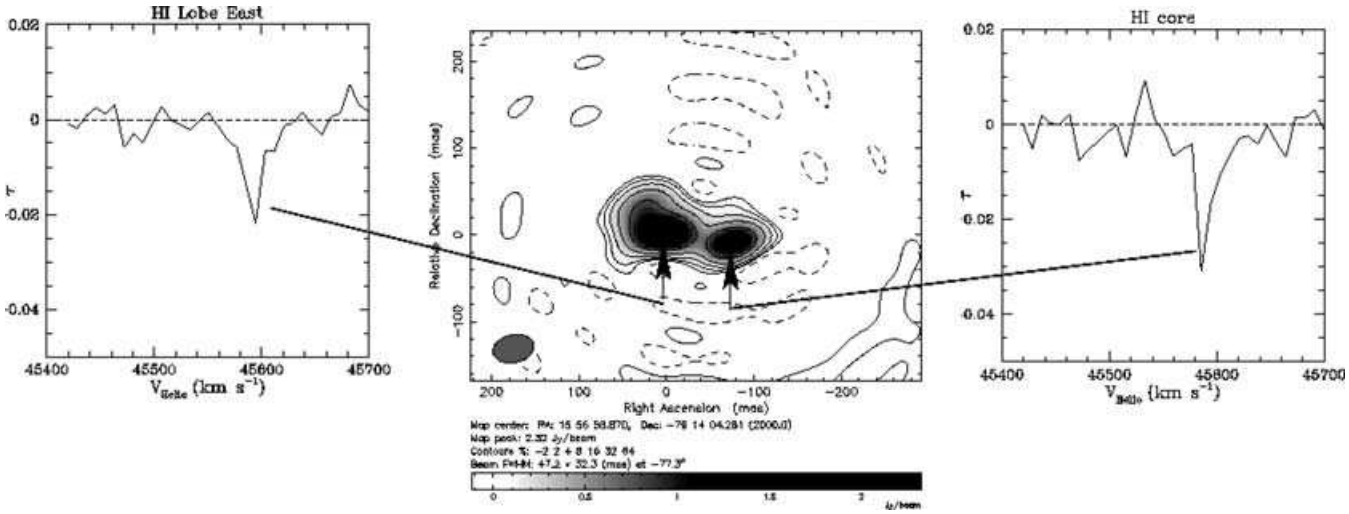

Figure 11. Middle: 1.23-GHz LBA continuum image of PKS 1549−79 obtained from the line-free channels. Right-hand side: integrated profile of the H I absorption in the western core source. Left-hand side: integrated profile of the H I absorption for the eastern jet source.

be boosted relative to the situation in which the jet is close to the plane of the sky. Therefore, although the total radio power of PKS 1549−79 uncorrected for beaming ($P_{2.3\,\mathrm{GHz}} = 5.4 \times 10^{26}$ W Hz^{-1}) would lead to its classification as a powerful radio galaxy that would normally appear as a Fanaroff–Riley type II (FR II) radio source if orientated close to the plane of the sky, the true (unbeamed) radio power of the source could be much lower. If we assume that the radio flux not recovered in the VLBI maps (i.e. 5 per cent of the total) represents an unbeamed radio component, this leads to a lower limit on the total unbeamed radio power of $P_{2.3\,\mathrm{GHz}} = 2.7 \times 10^{25}$ W Hz^{-1} – just above the break in the radio luminosity function (Auriemma et al. 1977) and in the transition region between Fanaroff–Riley type I (FR I) and FR II sources (Fanaroff & Riley 1974).

Assuming that the one-sided nature of the jet is a consequence of beaming effects, we can use the lower limit on the jet-to-counter-jet ratio (R_{jc}) derived from the radio maps to estimate the inclination of the jet to the line of sight. The 21-cm LBA continuum map (see Fig. 11) is the most sensitive for the detection of extended jet features close to the nucleus. The peak flux in the jet detected in this map is 2.3 Jy beam^{-1}, whereas the 3σ detection limit for the counter jet is 48 mJy beam^{-1}. Therefore, a lower limit on the jet-to-counter-jet ratio is $R_{\mathrm{jc}} \geqslant 48$. The jet-to-counter-jet ratio is related to the bulk Lorentz factor in the jet (γ) and the inclination of the jet to the line of sight (i) by

$$\cos(i) = \left(\frac{\gamma^2}{\gamma^2 - 1}\right)^{1/2} \left[\frac{R_{\mathrm{jc}}^{1/(2-\alpha)} - 1}{R_{\mathrm{jc}}^{1/(2-\alpha)} + 1}\right], \quad (1)$$

where α is the spectral index of the jet continuum emission. For $\alpha = -1$ and $R_{\mathrm{jc}} \geqslant 48$, we estimate an upper limit on the inclination of $i < 55^\circ$, assuming that the Lorentz factor for the bulk motion of the jet falls within the typical range estimated for extragalactic radio jets ($5 < \gamma < 10$).

An alternative possibility is that the one-sided jet is a consequence of a stronger interaction between the radio jet and the interstellar medium on the east side of the nucleus that leads to local re-acceleration of the electrons and enhanced radio emission; a strong jet–cloud interaction would also explain the curvature in the jet. However, this scenario would not account for the relative strength of the flat spectrum core and the fact that the asymmetric character of jet extends into the near-jet close to the core, as is clear from the higher resolution 2.3-GHz map (Fig. 10, middle).

3.4.2 H I 21-cm kinematics

Given the core-jet character of the radio continuum structure, which suggested that the jet is pointing close to our line of sight, it was a surprise to detect H I absorption in our ATCA observations (Morganti et al. 2001). On the basis of the simplest versions of the unified schemes, one would normally expect a relatively unobscured view of the quasar nucleus from the direction of the radio jet (Barthel 1989). The absorption in the spatially integrated radio emission has a FWHM ~ 80 km s^{-1}, and the peak optical depth is about 2 per cent. This leads to a column density of $(4.0 \pm 0.5) \times 10^{18} T_{\mathrm{spin}}$ cm^{-2}, where T_{spin} is the H I spin temperature. A possible interpretation described in Tadhunter et al. (2001) is that the H I absorption is associated with a dusty cocoon around the nucleus that also emits the narrow emission-line component, and is responsible for the obscuration of the quasar nucleus.

The new LBA data provide information about the spatial structure of the H I absorption. Fig. 11 shows the profiles of the H I absorption measured at the locations of both the core and the jet structures. Consistent with the idea of a foreground absorbing screen proposed by Morganti et al. (2001) and Tadhunter et al. (2001), the H I absorption was detected against both of the major radio components with similar redshift, linewidth and optical depth. Therefore, the diameter of the H I absorbing region is >120 mas (>286 pc). Note that the narrow H I absorption is significantly blueshifted (by $\sim$75 km s^{-1}) relative to the narrow optical emission lines (see Fig. 4 and Table 2), but this blueshift is an order of magnitude smaller than that measured in the [O III] lines, and might be attributed to gravitational motions if the absorbing cloud has not yet settled into the circumnuclear disc.

In Fig. 12, the H I absorption profile from the ATCA observations (from Morganti et al. 2001) is superimposed on the integrated absorption profile obtained from the new LBA observations. This shows that most of the H I absorption is recovered in the high spatial resolution LBA observations, and that the H I kinematics in the LBA and ATCA are consistent.

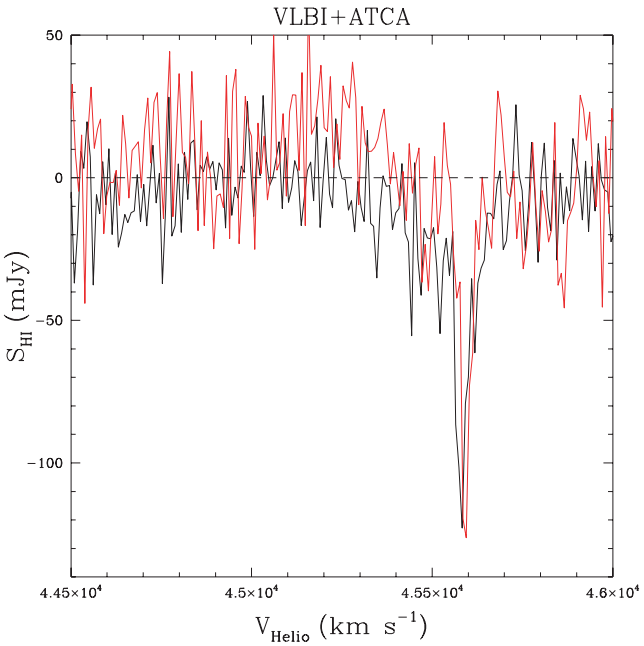

Figure 12. Profile of the H I absorption in PKS 1549−79. The black line represents the ATCA data of Morganti et al. (2001), while the red line represents the integrated H I profile measured from the new LBA data. Most of the absorbed flux is recovered in the higher resolution LBA observations.

4 DISCUSSION

4.1 Evolutionary status and the triggering of the activity

The ready detection of multiple tidal tails at a relatively high surface brightness level is entirely consistent with the idea that the activity in PKS 1549−79 has been triggered in a major merger between galaxies, at least one of which was gas rich and had a cold disc component prior to the merger. Indeed, the tail structure observed in PKS 1549−79, with two near-parallel tails pointing to the south and a jet-like structure pointing to the north bears marked similarity with the structures produced in numerical simulations by Barnes & Hernquist (1996) of the merger between two disc galaxies, observed from the orbital plane of the merging galaxies. In such a merger, it will take of the order of 500 Myr for the nuclei of the two galaxies to finally merge together. Therefore, it is likely that we are observing the system a considerable period after the start of the encounter.

The YSP provide useful complementary information about the merger. The presence of a reddened YSP in the nuclear regions of this object is consistent with the idea that the merger also triggered a starburst. Given that the YSP has an estimated age of 50–250 Myr at the observation epoch, it is likely that the starburst was triggered a considerable period after the start of the merger sequence. This in turn suggests that one of the galaxies had a significant bulge that hindered the formation of a bar that would otherwise lead to the major merger-induced star formation occurring early in the merger (Mihos & Hernquist 1996). Notwithstanding the uncertainties about the heating mechanism for the dust emitting the far-IR radiation, the substantial far-IR excess in this source suggests the presence of substantial ongoing star formation in the nuclear regions that is simultaneous with the currently observed quasar and jet activity.

It is also interesting to consider at what stage the radio source was triggered in the merger sequence. Tadhunter et al. (2001) have argued that since the extreme forbidden emission-line widths measured in PKS 1549−79 are only detected in radio galaxies with young, compact radio sources, it is likely that we are observing the radio source at a relatively early stage after the triggering of the activity ($<10^6$ yr). If this is correct, it is plausible that there was a significant delay (>40 Myr) between the starburst associated with the YSP detected at optical wavelengths and the triggering of the radio jet activity. However, the evidence for such a time delay is weaker in PKS 1549−79 than for some other radio sources in which the time lag between the major episode of merger-induced star formation and the triggering of the currently observed radio source is estimated as 0.3–2.0 Gyr (Johnston et al. 2005; Tadhunter et al. 2005; Emonts et al. 2006).

4.2 The nature of the AGN

Our new data provide key information about the nature of the AGN in PKS 1549−79. Most notably, the relatively narrow Paα detected in the quasar component of PKS 1549−79 (FWHM = 1940 ± 50 km s^{-1} from a single Gaussian fit) is consistent with the classification of this source as a narrow-line Seyfert 1 galaxy (NLS1; FWHM < 2000 km s^{-1}; Osterbrock & Pogge 1985; Osterbrock 1987) or more accurately, given its luminosity, a narrow-line quasar. Interestingly, the extreme blueshift of the [O III] line relative to the galaxy rest frame in this object is also similar to those detected in the broad [O III] emission-line components of many NLS1 galaxies and similar objects (Veron-Cetty, Veron & Goncalves 2001; Zamanov et al. 2002; Aoki, Kawaguchi & Ohta 2005; Boroson 2005).

NLS1 are often interpreted as AGN that are accreting at a relatively high Eddington radio ($L_{\rm bol}/L_{\rm edd} \sim 1$), based on the small virial black hole mass estimates deduced from their relatively narrow permitted linewidths (Pounds, Done & Osborne 1995; Mathur 2000; Mathur & Grupe 2005). It has also been suggested that the NLS1 fall significantly below the correlations between black hole mass and host galaxy bulge properties (Grupe & Mathur 2004). However, it is important to add the caveats that (i) the small permitted linewidths of NLS1 may reflect orientation effects (e.g. BLR disc viewed face on) rather than low black hole masses; and (ii) the bulge properties for NLS1 in the Grupe & Mathur (2004) study were deduced from [O III] linewidths, which are likely to be affected by non-gravitational (radial) motions suggested by the large [O III] blueshifts detected in some sources.

It is interesting to consider whether PKS 1549−79 is also a high accretion rate object with a large Eddington ratio. Its black hole mass can be estimated using two independent methods. First, a virial mass estimate can be obtained using the Paα linewidth and luminosity. Assuming the minimum extinction for Paα ($A_k = 0.74$ mag), and a Paα/Hβ ratio set at the case B recombination value (Paα/Hβ = 0.332; see Osterbrock 1989), we deduce an intrinsic quasar Hβ luminosity of $L(\mathrm{H}\beta) = 1.0 \times 10^{43}$ erg s^{-1} for our adopted cosmology. Assuming that FWHM (Hβ) = FWHM (Paα) = 1940 km s^{-1}, we then use the relationship between FWHM (Hβ), L(Hβ) and $M_{\rm bh}$ published by Greene & Ho (2005, their equation 7) to estimate a virial black hole mass of $M_{\rm bh} = 5.3 \times 10^7$ M$_\odot$. A second black hole mass estimate can be obtained from the correlation between R-band bulge luminosity (M_R) and black hole mass published by McLure & Dunlop (2002) along with the published R-band absolute magnitude for PKS 1549−79 (Drake et al. 2004a; $M_R = -21.9$ for our

cosmology).[1] This leads to $M_{\rm bh} = 2.6 \times 10^8$ M$_\odot$ – almost an order of magnitude larger than the virial estimate of black hole mass. However, the *R*-band luminosity estimate can be regarded as an upper limit because the YSP in the bulge and tail features of PKS 1549−79 along with any AGN contamination are likely to artificially boost the *R*-band luminosity; the only way in which the *R*-band magnitude can substantially underestimate the black hole mass is if the host galaxy as a whole is subjected to substantial intrinsic extinction. In contrast, the virial estimate is likely to represent a lower limit on the black hole mass because of the effects of orientation on the Paα linewidth, especially given that the radio observations suggest that radio jet is pointing close to the line of sight, with the putative BLR disc observed close to face-on. The true mass of the black hole in PKS 1549−79 is therefore likely to fall between the virial and bulge luminosity estimates.

The other element required to determine the Eddington ratio is the bolometric luminosity ($L_{\rm bol}$) of the quasar. $L_{\rm bol}$ can be estimated using the quasar continuum modelling results along with information on generic quasar spectral energy distributions (SEDs) presented in Elvis et al. (1994). The range of optical SEDs that is consistent with our optical/IR spectroscopy and imaging have monochromatic *V*-band luminosities in the range $1.2 \times 10^{41} < L_V < 4.8 \times 10^{42}$ erg s^{-1} Å^{-1} or $6.6 \times 10^{44} < \lambda L_\lambda < 2.6 \times 10^{46}$ erg s^{-1} ($\lambda = 5500$ Å) for the quasar in PKS 1549−79. The *V*-band bolometric correction factor listed in Elvis et al. (1994) is $L_{\rm bol}/(\lambda L_V) = 14.2$. Therefore, we estimate that the bolometric luminosity of PKS 1549−79 falls in the range $9.0 \times 10^{45} < L_{\rm bol} < 3.8 \times 10^{47}$ erg s^{-1}. Note that, although the radio jet in this source is pointing close to our line of sight, there is no evidence that the optical/IR continuum is substantially affected by contamination by a beamed synchrotron source: not only does the SED of PKS 1549−79 show a steep decline between radio and sub-mm wavelengths [compare Drake et al. (2004b) with Beasley et al. (1997)], but both the Hβ equivalent width and the $L_{\rm bol}/L_{\rm ir}$ ratio also fall well within the range measured for unbeamed quasars.

These estimates of $L_{\rm bol}$ lead to Eddington ratios in the range $0.3 < L_{\rm bol}/L_{\rm edd} < 11$ for our upper estimate of the black hole mass ($M_{\rm bh} = 2.6 \times 10^8$ M$_\odot$) and in the range $1.3 < L_{\rm bol}/L_{\rm edd} < 57$ for our lower estimate of the black hole mass ($M_{\rm bh} = 5.3 \times 10^7$ M$_\odot$). The measurement of such high Eddington ratios reinforces the link between PKS 1549−79 and NLS1 galaxies.

Although we cannot rule out the idea that PKS 1549−79 is a significant outlier relative to the statistical correlations we have used to derive both black hole mass and bolometric luminosity estimates, our results are at least consistent with accretion at a high Eddington ratio in this object. On this evidence, accretion at high Eddington ratio does not prevent the formation of powerful, relativistic jets. For comparison, the Eddington ratio measured for Cygnus A – the only quasar with a direct, dynamical black hole mass estimate – is (1.6–6.0)$\times 10^{-2}$ (Tadhunter et al. 2003). Similarly, Dunlop et al. (2003) derive relatively small Eddington ratios (typically $L_{\rm bol}/L_{\rm edd} < 0.1$) based on *R*-band black hole mass estimates of several radio-loud and radio-quiet quasars. On the other hand, Punsly & Tingay (2005) have recently highlighted the high-redshift quasar PKS 0743−67 as another object that is accreting at high Eddington ratio but has powerful radio jets.

[1] Note that the *R*-band absolute magnitude derived by Drake et al. (2004a) is based in the integrated light measured within the outermost ellipse fitted to their *R*-band image (corresponding to a semimajor axis of 12.5 arcsec or 30 kpc). Since this magnitude corresponds to the total light, and no disc/bulge separation has been attempted, it is likely to *overestimate* the luminosity of the bulge.

4.3 Characterizing the warm outflow

Recent theoretical studies of galaxy evolution have invoked quasar-induced outflows to explain both the correlations between the masses of black holes and the galaxy bulge properties (e.g. Silk & Rees 1998; Fabian 1999; di Matteo et al. 2005), and the form of the galaxy luminosity function at the high-luminosity end (e.g. Benson et al. 2003). Such feedback models require that a relatively large fraction of the available accretion power of the quasars is thermally coupled to the circumnuclear ISM (∼10 per cent; Fabian 1999; di Matteo et al. 2005).

PKS 1549−79 appears to represent a situation close to that modelled in some of the recent simulations (e.g. di Matteo et al. 2005), in which the black hole is growing rapidly via merger-induced accretion following a merger between gas-rich galaxies. We have also found – in the blueshifted [O III] lines – clear evidence for an outflow in the central regions of this source. Therefore, it is important to investigate whether the properties of the warm gas outflow in PKS 1549−79 are consistent with the assumptions of the quasar feedback models.

We start by determining the mass outflow rate in the intermediate (blueshifted) component. For a steady-state outflow, the mass outflow rate is given by

$$\dot{M} = N \epsilon v_{\rm out} A m_{\rm p}, \tag{2}$$

where N is the electron density, ϵ the volume filling factor, $v_{\rm out}$ the outflow velocity, A the area of the outflow and $m_{\rm p}$ the mass of the proton. The filling factor is related to the Hβ luminosity [L(Hβ)], density and emitting volume V as follows:

$$\epsilon = \frac{L({\rm H}\beta)}{\alpha^{\rm eff}_{{\rm H}\beta} h \nu_{{\rm H}\beta} N V}, \tag{3}$$

where $\alpha^{\rm eff}_{{\rm H}\beta}$ is the effective Hβ recombination coefficient (see Osterbrock 1989), $\nu_{{\rm H}\beta}$ the frequency of Hβ and h the Planck constant. It follows that the mass outflow rate can be written as

$$\dot{M} = \frac{L({\rm H}\beta) m_{\rm p} v_{\rm out} A}{\alpha^{\rm eff}_{{\rm H}\beta} h \nu_{{\rm H}\beta} N V}, \tag{4}$$

and for a spherical outflow this reduces to

$$\dot{M} = \frac{3 L({\rm H}\beta) m_{\rm p} v_{\rm out}}{N \alpha^{\rm eff}_{{\rm H}\beta} h \nu_{{\rm H}\beta} r}, \tag{5}$$

where r is the radius of the spherical volume. On the basis of our spectroscopy, we estimate an Hβ luminosity of $L({\rm H}\beta) = 2.8 \times 10^{40}$ erg s^{-1} for the intermediate, blueshifted component and a rest-frame outflow velocity of $v_{\rm out} = 680$ km s^{-1}. If we assume case B recombination theory for an electron temperature $T = 10\,000$ K and that the spherical outflow has the same radius as the radio source (180 mas or $r = 430$ pc for our cosmology), we find that the mass outflow rate in units of solar masses per year is given by

$$\dot{M} = 9.1 \left(\frac{10^2 \, {\rm cm}^{-3}}{N} \right) \, {\rm M}_\odot \, {\rm yr}^{-1}. \tag{6}$$

The largest uncertainty in this calculation is the electron density of the outflowing gas (N). Because it has not been possible to measure the electron density for the outflowing gas directly in the case of PKS 1549−79, we assume that it falls in the range measured for the NLR of other radio galaxies. The typical electron densities measured for kpc-scale ionized gas in extended radio sources such as Cygnus A

(Taylor, Tadhunter & Robinson 2003) and 3C321 (Robinson et al. 2000) are $N \sim 10^2$ cm^{-3}. However, the densities may be larger in the emission-line regions associated with compact radio sources, and in the case of PKS 1345+12 – a similar object that has broad, blueshifted [O III] lines – a relatively high electron density ($N > 5 \times 10^3$ cm^{-3}) has been deduced for the blueshifted emission-line components (Holt et al. 2003). Therefore, it is reasonable to assume densities in the range $10^2 < N < 10^4$ cm^{-3}, leading to mass outflow rates $0.12 < \dot{M} < 12 M_{\odot} \mathrm{yr}^{-1}$. It is notable that this covers same range as the mass outflow rates deduced for the NLR of Seyfert galaxies (Veilleux, Cecil & Bland-Hawthorn 2005) and the high-ionization absorption-line systems detected at UV and X-ray wavelengths in some AGN (Crenshaw et al. 2003), but is somewhat less than deduced for the neutral outflows detected in extreme starburst sources such as ULIRGs (Rupke, Veilleux & Sanders 2005a, b). For the same range of densities, we estimate that the total mass in the warm gas outflow falls in the range $1.9 \times 10^4 < M_{\mathrm{total}} < 1.9 \times 10^6 M_{\odot}$ and the filling factor falls in the range $2.3 \times 10^{-3} < \epsilon < 2.3 \times 10^{-7}$.

From the point of view of gauging the likely impact of the warm gas outflow on the circumnuclear gas in the bulge of the host galaxy of PKS 1549−79, it is also important to estimate the kinetic power of the outflow, including both the radial and turbulent components in the gas motion. Assuming that the relatively large linewdith of the outflowing gas reflects a turbulent motion that is present at all locations in the outflow region, the kinetic power is

$$\dot{E} = 6.34 \times 10^{35} \frac{\dot{M}}{2} \left(v_{\mathrm{out}}^2 + (\mathrm{FWHM})^2 / 1.85 \right) \mathrm{erg\ s}^{-1}, \quad (7)$$

where FWHM is the full width at half-maximum of the blueshifted [O III] line in km s^{-1}, and $\dot{M}$ is the mass outflow rate expressed in solar masses per year. For $v_{\mathrm{out}} = 680$ km s^{-1}, FWHM = 1282 km s^{-1} and the mass outflow rates determined above, we find that the kinetic power for the outflowing gas falls in the range $5.1 \times 10^{40} < \dot{E} < 5.1 \times 10^{42}$ erg s^{-1}. Taking the Eddington luminosity derived from the larger black hole mass estimate (see Section 4.2 above) as an estimate of the total power available from accretion, the kinetic power in the warm gas component represents only a small fraction ($1.6 \times 10^{-6} < \dot{E}/L_{\mathrm{edd}} < 1.6 \times 10^{-4}$) of the available accretion power, in contrast to the quasar feedback models which require a much larger fraction of the accretion power of the black hole to be thermally coupled to the gas surrounding the black hole. It is also unlikely that the warm gas outflow by itself is capable of removing all the warm/cool gas from the central regions of the host galaxy. Assuming that PKS 1549−79 has a total mass $M_{\mathrm{total}} \sim 10^{11} M_{\odot}$, and a gas mass $M_{\mathrm{gas}} \sim 10^{10} M_{\odot}$ contained within a radius of 5 kpc – conservative assumptions for ULIRGs which are likely to have a larger gas mass concentrated within a smaller radius – the gravitational binding energy of the gas is $E_{\mathrm{bind}} \approx G M_{\mathrm{gas}} M_{\mathrm{total}} / R_{\mathrm{gas}} \approx 2 \times 10^{58}$ erg. In comparison, the warm gas outflow will deposit only $\sim 10^{55}$–10^{57} erg into the surrounding ISM, assuming that it can persist in its current form for the typical 10^7 yr lifetime of an extragalactic radio source.

How do we explain the fact that the estimated kinematic power in the warm gas outflow in PKS 1549−79 is at least three orders of magnitude less than might be expected on the basis of the quasar feedback models? Considering first the assumptions that have gone into the above estimates, the key parameters are the radius of the outflow, the electron density and the emission-line luminosity. $\dot{E}$ would be underestimated if the radius and/or density of the outflow have been overestimated, or the Hβ luminosity has been underestimated. However, it is unlikely that the radius of the outflow region has been overestimated, because recent *HST* imaging observations of PKS 1549−79 demonstrate that it has a similar scale to the radio source (Batcheldor et al., in preparation); allowing for projection effects, it is more likely that the radius we have used is conservative and the outflow region is significantly *larger* than we have estimated. Similarly, given that warm gas has been accelerated to large velocities and other compact radio sources show strong evidence for a relatively high-density NLR (Holt et al. 2003; Holt 2005), it is unlikely that the electron density in the outflow can be substantially less than the measured density in the narrow component (430 ± 50 cm^{-3}) and the lower limit ($N \geqslant 10^2$ cm^{-3}) we have assumed.

Given the fact that the quasar nucleus in PKS 1549−79 is itself substantially obscured at optical wavelengths, it is less easy to dismiss the idea that a portion of the outflow region is highly extinguished at optical wavelengths so that the Hβ luminosity is underestimated. However, it is unlikely that the Hβ has been underestimated by more than a factor of 50 because the blueshifted outflow component would then make a substantial contribution to the Paα flux, which is not observed.

Most plausibly, the warm gas outflow we have detected in [O III] represents only a small fraction of the total mass in the outflow, with the remaining mass locked in hotter or cooler phases of the ISM that are difficult to detect at optical wavelengths. Recently, Morganti et al. (2003, 2005a) and Morganti, Tadhunter & Oosterloo (2005b) have detected massive *neutral* outflows in several compact radio sources using observations of the 21-cm line of neutral hydrogen. The mass outflow rates and energy fluxes contained within such neutral outflows are substantially larger than we have estimated for the warm gas outflow in PKS 1549−79. It is notable that there is a hint of a blue wing to the H I 21-cm line detected in PKS 1549−79 (see Figs 11 and 12). If this can be confirmed with higher quality observations, it may be possible to make a more complete census of the warm and cool gas outflows in this object.

4.4 H I spin temperature

The exact value of the H I spin temperature (T_{spin}) is a major uncertainty in calculating the column density of neutral hydrogen using H I 21-cm absorption-line observations. Although T_{spin} is often assumed to have values consistent with those estimated in the Galaxy ($100 < T_{\mathrm{spin}} < 1000$ K; Heiles & Kulkarni 1988), higher values may be appropriate in the central regions around AGN because of excitation of the upper level of the 21-cm hyperfine transition by collisions, Lyα photons or 21-cm continuum photons [see Bahcall & Ekers (1969) for a discussion]. The latter may be particularly important in a case like PKS 1549−79 because the radio emission is beamed towards the H I absorbing cloud along our line of sight. However, to our knowledge there have so far been no direct estimates of the H I 21-cm spin temperature in the vicinity of luminous AGN.

PKS 1549−79 provides an excellent opportunity to estimate the spin temperature directly because we have an independent estimate of the neutral column towards the quasar nucleus from the extinction estimates derived from our quasar continuum modelling. The SED modelling gives $2.0 < E(B-V) < 4.0$ for the intrinsic line of sight reddening towards the quasar nucleus. Assuming the standard Galactic dust-to-gas ratio [$E(B-V)/N_{\mathrm{HI}} = 1.7 \times 10^{-22}$ mag cm^{-2}; Bohlin, Savage & Drake 1978], this translates into neutral H I columns in the range $1.2 \times 10^{22} < N_{\mathrm{HI}} < 2.4 \times 10^{22}$ cm^{-2}. On the basis of our H I 21-cm absorption-line measurements, the neutral H I column is related to the spin temperature by $N_{\mathrm{HI}} = (4.0 \pm 0.5) \times 10^{18} T_{\mathrm{spin}}$ cm^{-2}. Therefore, by combining the estimates of

the neutral H I column derived from both the H I 21 cm and the quasar SED measurements we find that the electron spin temperature must fall in the range $3000 < T_{\rm spin} < 6000$ K. These measurements provide clear evidence that the H I spin temperature in PKS 1549−79 is higher than the typical Galactic value.

Implicit in our estimate of $T_{\rm spin}$ is the assumption that the column reddening the quasar is the same as that causing the H I 21-cm absorption. Although the quasar nucleus can be considered point-like, while the radio emission is clearly spatially extended in our VLBI observations, our LBA observations show that the H I absorption covers the entire spatially resolved radio source, including the flat spectrum core to the western jet of the source. Therefore, it is entirely plausible that the H I 21 cm and quasar reddening columns are associated with the same cloud. Another major assumption we have made is that the dust-to-gas ratio in the absorbing cloud has the Galactic value. This is called into question by recent observations that provide evidence for dust-to-gas ratios in the vicinity of AGN that are a factor of ∼10 or more *lower* than the Galactic value (Maiolino et al. 2001). However, if such low dust-to-gas ratios also hold in PKS 1549−79, the resulting spin temperature would be even larger than we have estimated above, further strengthening the evidence for large $T_{\rm spin}$ in this object. In view of this, the lower limit we have derived for the spin temperature in PKS 1549−79 ($T_{\rm spin} > 3.0 \times 10^3$ K) is likely to be conservative.

5 CONCLUSIONS AND FURTHER WORK

The new observations presented in this paper confirm that PKS 1549−79 represents a luminous quasar observed at an early stage of its evolution. The quasar and jet activity have been triggered in a major merger which has also triggered substantial star formation. Accreting at close to the Eddington rate, the black hole in this system is growing rapidly and simultaneously driving relativistic jets. The growth phase of the black hole is substantially obscured at optical wavelengths in this object, consistent with recent galaxy evolution models (Hopkins et al. 2005). However, although the optical emission lines provide evidence for a high-ionization, warm outflow associated with the AGN, the warm outflow currently observed at optical wavelengths is not in itself sufficient to remove all the gas from the central regions of the galaxy.

PKS 1549−79 is a key object because it links together several classes of active galaxies, including radio galaxies, quasars, ULIRGs, NLS1 and AGN with high-ionization absorption-line systems. Moreover, it shows many properties in common with the recently discovered population of high-redshift AGN detected at sub-mm wavelengths (Alexander et al. 2005). The common thread is that all these classes of object are associated with the triggering and feedback effects of major galaxy mergers. Although much attention is paid to the links between star formation and activity in objects at high redshift, this study of PKS 1549−79 serves to emphasize that some galaxies are evolving rapidly in the local universe, and that it is possible to use such objects to study the co-evolution of black holes and galaxy bulges in depth.

Several further observational studies of PKS 1549−79 would enhance our understanding of the relationship(s) between AGN activity and galaxy evolution. They include the following.

(i) Near-IR measurements of the stellar bulge luminosity and velocity dispersion to improve estimates of the black hole mass.

(ii) High-quality optical spectroscopy observations of a wider range of emission-line diagnostics to measure the electron density accurately, and thereby improve our determination of the properties of the warm gas outflow.

(iii) Deep X-ray spectroscopy observations to refine estimates of the quasar bolometric luminosity and absorbing H I column. Such observations would also allow the links between PKS 1549−79, NLS1 and sub-mm galaxies to be further investigated.

(iv) Multi-epoch VLBI observations to search for superluminal motions in the jet, and accurately determine the inclination of the jet to the line of sight.

(v) Deeper H I 21-cm measurements and high-resolution optical observations of the NaID line to investigate the importance of neutral gas outflows.

ACKNOWLEDGMENTS

Based on observations collected at the ESO, Chile [ESO Programmes 69.B-0548(A), 71.B-0320(A) and 72.B-0792(A)] and the Anglo-Australian Observatory, Siding Spring, Australia. KJI, JH and MB acknowledge financial support from PPARC. Edward King (CSIRO) provided original images made with the SHEVE network. We thank the anonymous referee for useful comments. The LBA is part of the Australia Telescope, funded by the Commonwealth of Australia for operation as a National Facility managed by CSIRO and the University of Tasmania.

REFERENCES

Alexander D. M., Smail I., Bauer F. E., Chapman S. C., Blain A. W., Brandt W. N., Ivison R. J., 2005, Nat, 434, 738
Aoki K., Kawaguchi T., Ohta K., 2005, ApJ, 618, 601
Aretxaga I., Terlevich E., Terlevich R. J., Cotter G., Diaz A. I., 2001, MNRAS, 325, 636
Auriemma C., Perola G. C., Ekers R. D., Fanti R., Lari C., Jaffe W. J., Ulrich M. H., 1977, A&A, 57, 41
Bahcall J. N., Ekers R. D., 1969, ApJ, 157, 1055
Barnes J. A., Hernquist L., 1996, ApJ, 471, 115
Barthel P. D., 1989, ApJ, 336, 606
Baum S. A., Heckman T., van Breugel W., 1990, ApJS, 74, 389
Beasley A. J., Conway J. E., Booth R. S., Nyman L.-A., Holdaway M., 1997, A&AS, 124, 469
Bellamy M. J., Tadhunter C. N., Morganti R., Wills K. A., Holt J., Taylor M. D., Watson C. A., 2003, MNRAS, 344, L80
Benson A. J., Bower R. G., Frenk C. S., Lacey C. G., Baugh C. M., Cole S., 2003, ApJ, 599, 38
Bessell M. S., Castelli F., Plez B., 1998, A&A, 333, 231
Binette L., Wilson A. S., Storchi-Bergmann T., 1996, A&A, 312, 365
Bohlin R. C., Savage B. D., Drake J. F., 1978, ApJ, 224, 132
Boroson T., 2005, ApJ, 130, 381
Bruzual G., Charlot S., 2003, MNRAS, 344, 1000
Clark B. G., 1973, Proc. IEEE, 61, 1242
Clark N., 1996, PhD thesis, Univ. Sheffield
Clark N. E., Axon D. J., Tadhunter C. N., Robinson A., O'Brien P., 1998, ApJ, 494, 546
Cohen R. O., Osterbrock D. E., 1981, ApJ, 243, 81
Costero R., Osterbrock D. E., 1977, ApJ, 211, 675
Crenshaw D. M., Kraemer S. B., George I. M., 2003, ARA&A, 2003
Dickson R. D., 1997, PhD thesis, Univ. Sheffield
Dickson R., Tadhunter C., Shaw M., Clark N., Morganti R., 1995, MNRAS, 273, L29
di Matteo T., Springel V., Hernquist L., 2005, Nat, 433, 604
Dopita M., Sutherland R. S., 1995, ApJ, 455, 468
Dopita M., Sutherland R. S., 1996, ApJS, 102, 161
Drake C. L., McGregor P. J., Dopita M. A., 2004a, AJ, 128, 955
Drake C. L., Bicknell G. V., McGregor P. J., Dopita M. A., 2004b, ApJ, 128, 969

Dunlop J. S., Peacock J. A., 1990, MNRAS, 247, 19
Dunlop J. S., McClure R. J., Kukula M. J., Baum S. A., O'Dea C. P., Hughes D. H., 2003, MNRAS, 340, 1095
Emonts B. H. C., Morganti R., Tadhunter C. N., Holt J., Oosterloo T. A., van der Hulst J. M., Wills K. A. 2006, A&A, in press
Elvis M. et al., 1994, ApJS, 95, 1
Fabian A. C., 1999, MNRAS, 308, L39
Fanaroff B. L., Riley J. M., 1974, MNRAS, 167, 31
Grandi S. A., Osterbrock D. E., 1978, ApJ, 220, 783
Greene J. E., Ho L. C., 2005, ApJ, 630, 122
Grupe D., Mathur S., 2004, ApJ, 606, L41
Heckman T. M., Smith E. P., Baum S. A., van Breugel W. J. M., Miley G. K., Illingworth G. D., Bothun G. D., Balick G. D., 1986, ApJ, 311, 526
Heiles C., Kulkarni S., 1988, in Kellerman K., Vershurr G., eds, Galactic & Extragalactic Radio Astronomy, Kluwer, Berlin, p. 95
Holt J., 2005, PhD thesis, Univ. Sheffield
Holt J., Tadhunter C. N., Morganti R., 2003, MNRAS, 342, 995
Hopkins P. F., Hernquist L., Cox T. J., di Matteo T., Martini P., Robertson B., Springel V., 2005, ApJ, 630, 705
Jauncey D. L., The SHEVE Team, 1994, in Robertson J. G., Tango W. J., eds, Very High Angular Resolution Imaging, IAU158. Kluwer, Dordrecht, p. 131
Johnston H. M., Hunstead R. W., Cotter G., Sadler E. M., 2005, MNRAS, 356, 515
Kauffmann G., Haehnelt M., 2000, MNRAS, 311, 576
Madau P., Ferguson H. C., Dickinson M. E., Giavalisco M., Steidel C. C., Fruchter A., 1996, MNRAS, 283, 1388
Maiolino R., Marconi A., Salvati M., Risaliti G., Severgnini P., Oliva E., La Franca F., Vanzi L., 2001, A&A, 365, 28
Mathur S., 2000, MNRAS, 314, L17
Mathur S., Grupe D., 2005, A&A, 432, 436
McLure R. J., Dunlop J. S., 2002, MNRAS, 331, 795
Mihos C. J., Hernquist L., 1996, 464, 641
Morganti R., Robinson A., Fosbury R. A. E., di Serego Alighieri S., Tadhunter C. N., Malin D. F., 1991, MNRAS, 249, 91
Morganti R., Oosterloo T., Tadhunter C. N., 2001, MNRAS, 323, 331
Morganti R., Oosterloo T., Emonts B. H. C., van der Hulst J. M., Tadhunter C. N., 2003, ApJ, 593, L69
Morganti R., Oosterloo T. A., Tadhunter C. N., van Moorsel G., Emonts B., 2005a, A&A, 439, 521
Morganti R., Tadhunter C. N., Oosterloo T. A., 2005b, A&A, 444, L9
Osterbrock D. E., 1987, Lecture Notes Phys., 307, 1
Osterbrock D. E., 1989, The Astrophysics of Gaseous Nebulae and Active Galactic Nuclei, University Science Books, Mill Valley, CA
Osterbrock D. E., Pogge R. W., 1985, ApJ, 297, 166
Pounds K., Done C., Osborne J., 1995, MNRAS, 277, L5
Preston R. A., The SHEVE Team, 1993, in Davis R. J., Booth R. S., eds, Sub-Arcsecond Radio Astronomy, Cambridge Univ. Press, Cambridge, p. 428
Punsly B., Tingay S. J., 2005, ApJ, 633, L93
Rieke G. H., Lebofsky M. J., 1985, ApJ, 288, 618
Robinson T. G., Tadhunter C. N., Axon D. J., Robinson A., 2000, MNRAS, 317, 922
Rupke D. S., Veilleux S., Sanders D. B., 2005a, ApJ, 632, 751
Rupke D. S., Veilleux S., Sanders D. B., 2005b, ApJS, 160, 115
Sanders D. B., Mirabel I. F., 1996, ARA&A, 34, 749
Sault R. J., Teuben P. J., Wright M. C. H., 1995, in Shaw R., Payne H. E., Hayes J. J. E., eds, ASP Conf. Ser. Vol. 11, Astronomical Data Analysis Software & Systems IV, Astron. Soc. Pac., San Francisco, p. 433
Schlegel D. J., Finkbeiner D. P., Davis M., 1998, ApJ, 500, 525
Seaton M. J., 1979, MNRAS, 187, 73
Shepherd M. C., Pearson T. J., Taylor G. B., 1994, BAAS, 26, 987
Silk J., Rees M. J., 1998, A&A, 331, L1
Simpson C., Rawlings S., 2000, MNRAS, 317, 1023
Smith E. P., Heckman T. M., 1989, ApJ, 341, 658
Solorzano-Innarea C., 2001, PhD thesis, Univ. Sheffield
Storchi-Bergmann T., Wilson A. S., Mulchaey J. S., Binette L., 1996, A&A, 312, 357
Tadhunter C. N., Fosbury R. A. E., Quinn P. J., 1989, MNRAS, 240, 225
Tadhunter C., Scarrott S., Draper P., Rolph C., 1992, MNRAS, 256, 53P
Tadhunter C. N., Metz S., Robinson A., 1994, MNRAS, 268, 989
Tadhunter C. N., Dickson R. C., Shaw M. A., 1996, MNRAS, 281, 591
Tadhunter C. N., Wills K., Morganti R., Oosterloo T., Dickson R., 2001, MNRAS, 327, 227
Tadhunter C., Dickson R., Morganti R., Robinson T. G., Wills K., Villar-Martin M., Hughes M., 2002, MNRAS, 300, 977
Tadhunter C., Marconi A., Axon D., Wills K., Robinson T. G., Jackson N., 2003, MNRAS, 342, 861
Tadhunter C., Robinson T. G., Gonzalez Delgado R. M., Wills K., Morganti R., 2005, MNRAS, 356, 480
Taylor M. D., Tadhunter C. N., Robinson T. G., 2003, MNRAS, 342, 995
Tremaine S. et al., 2002, ApJ, 574, 740
Tzioumis A. et al., 2002, A&A, 392, 841
Veilleux S., Cecil G., Bland-Hawthorn J., 2005, ARA&A, 43, 769
Veron-Cetty M.-P., Veron P., Goncalves A. C., 2001, A&A, 372, 730
Villar-Martin M., Tadhunter C. N., Morganti R., Clark N., Kileen N., Axon D., 1998, A&A, 332, 479
Villar-Martin M., Tadhunter C. N., Morganti R., Axon D. J., Koekemoer A., 1999, MNRAS, 307, 24
Wills K. A., Tadhunter C. N., Robinson T. G., Morganti R., 2002, MNRAS, 333, 221
Wills K. A., Morganti R., Tadhunter C. N., Robinson T. G., Villar-Martin M., 2004, MNRAS, 347, 771
Zamanov R., Marziani P., Sulentic J. W., Calvani M., Dultzin-Hacyan D., Bachev R., 2002, ApJ, 576, L9

This paper has been typeset from a TEX/LATEX file prepared by the author.